Recent advancements in additive manufacturing technologies for porous material applications

Subhash Guddati[1] · A. Sandeep Kranthi Kiran[2,3,4] ◉ · Montray Leavy[1] · Seeram Ramakrishna[4]

Abstract

The fabrication of porous structures by additive manufacturing (AM) technologies has been broadly explored over the past few years. Based on the application, most of the research work in AM is focused on making high-density parts with porosity values ranging from 0.1 to 5%. Because of numerous technical challenges and lack of process control/monitoring, full aids of AM in porous application industries are not yet widespread in comparison with other technologies in the same arena. However, only very limited information is available on the exact correlation between process control and final 3D object, but this is rare. In 3D technology, the exact process parameters that user needs to adapt while processing his 3D object information are very limited. In this article, we have reviewed and critically analyzed present established AM technologies for fabricating porous parts, as well as post-processing characterization techniques and its applications in detail. In-depth analysis is done on different lattice structures and process parameters those are controlling the porosity of AM parts. We have also attempted to briefly discuss on the present porous applications in filtration and purification, energy, medical, and pharmaceutical domains.

1 Introduction

3D printing or additive manufacturing (AM) is a technology that creates objects/parts/components by adding thin layers of materials using additive processes rather than the more traditional subtractive techniques. As the entire process in AM is based on the progressive addition of materials, the approach enables minimal or zero wastage of material and also has a great control over geometrical design [1]. Since its

✉ Seeram Ramakrishna
seeram@nus.edu.sg

1   Entegris Asia Pte. Ltd, Singapore 417818, Singapore

2   Medical Materials Laboratory, Department of Metallurgical and Materials Engineering, Indian Institute of Technology Madras, Chennai 600036, India

3   Department of Biotechnology, Bhupat and Jyoti Mehta School of Biosciences, Indian Institute of Technology Madras, Chennai 600036, India

4   NUS Centre for Nanofibers and Nanotechnology, Department of Mechanical Engineering, National University of Singapore, 2 Engineering Drive 3, Singapore 117581, Singapore

introduction, a remarkable evolution has undergone in this segment by proving its capability to produce highly complex customized structures with great accuracy in the fields of aerospace, biomedical engineering, architecture, and automotive [2–4]. The exponential interest from industry, the research, and academic communities have elevated the AM parts from just prototypes to industry commercialization. AM technology is now broadly recognized as a new paradigm for design, and a powerful tool in many different fields of science such as architecture, manufacturing processes, aerospace engines, and bio-compatible materials. In general, AM fabrication process steps consist of (i) creating computer-aided design (CAD) model, (ii) generating stereolithography (STL) format file, (iii) slicing the design, (iv) creating tool path, (v) printing the design in the 3D printer, and (vi) finally post-processing. However, for lattice-designed porosity, an additional step in between slicing and tool path is being introduced to integrate the lattice structure design to the STL CAD model [5]. Schematic diagram of the process is shown in Fig. 1.

In AM, during the designing of 3D objects, it is very important to define upper limit/lower limit tolerances for each characteristic to ensure the part harmonizes with the application intended for. In this view, the amount of porosity
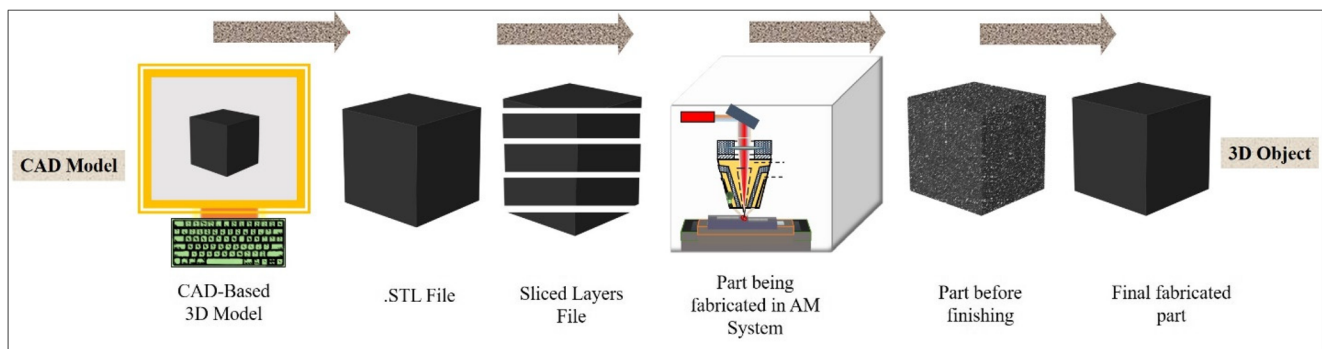
Fig. 1 General view of fabrication of objects by AM technologies

generated within the 3D-printed part is of a great area of interest. Both biomedical and high-strength applications need a different set of porosity requirements. Regardless of the fact that AM machineries allow the construction of intricate porous parts with a controlled architecture, changes in the part geometry can still happen between as-designed and as-fabricated morphological properties [6, 7]. As we know, the properties of the porous material hinge critically on its structure, which can significantly affect the mechanical response of the porous material, thereby defining the field of applications. In some cases, defects originating from the initial raw materials, process control parameters, and insufficient post-processing procedures can intensely influence structural integrity and robustness [8, 9]. In other cases, the porosity has a negative effect for structural load-bearing applications. For high-stress applications, to avoid mechanical failures, parts should be fully dense (< 1% porosity), whereas in biomedical applications, the amount of porosity within 3D parts has become an area of interest and is being considered a prerequisite in implant materials for better integration with biological tissues. A higher degree of porosity, especially for tissue regeneration and osseointegration, is sometimes necessary (> 25% porosity), and also, the kind of porosity is intentionally engineered into definite biomedical implantations [10–12]. The porosity in the 3D-printed part should be at a controlled level to withstand various amounts of mechanical and environmental stresses during its use. The on-growing demand for synthetic biomaterials for medical implants is mounting swiftly due to aging population globally.

To limit the scope, this paper aims to discuss only the development of porous structures in AM technologies and its connected sciences to it. To better understand the state of the art and its associated challenges, this paper will also summarize a large number of reported ways to generate 3D-printed porous materials processed by various AM techniques. Various characterization procedures for measuring the sample density and porosity in AM-printed parts are applied, compared, and critically discussed to develop and obtain accurate and precise measurements on porosity for future generations.

2 Additive manufacturing of porous parts

The importance of porosity assortment and structural gradients in biomedical engineering, filtration, purification, and energy applications has been increased exponentially in recent years. Current AM processes are now capable of inducing porosity at a very specific location in AM parts to alter the overall performance of the scaffolds and engineering applications. Stoffregen et al. classified the AM techniques for porous parts as (i) geometrically defined lattice structure porosity (GDLSP) and (ii) geometrically undefined porosity (GUP). Porosity and pore size of GDLSP are determined by different lattice structures and strut thickness respectively, whereas in GUP process, the desired porosity and pore size are achieved by optimizing the process parameters of AM technologies. Generally, GUP pore size ranges from 1 to 100 μm and GDLSP pore size lies between 100 μm and 1 mm. Figure 2 a shows the GUP type of porosity made by selective laser sintering (SLM) process of laser power optimization. The pore size achieved in this process is in the 10- to 30-μm range, and the porosity is achieved to its maximum level [13]. Figure 2 b describes the impact of SLM-fabricated GUP type of porosity by "layer thickness optimization." Porous materials of different layer thickness (0.1, 0.15, and 0.2 mm) were fabricated to compare and analyze the outcome of layer thickness on the porosity. It is found that the layer with maximum thickness (0.2 mm) achieved a maximum pore size of 43 μm. It is also understood that a larger layer thickness provides a higher porosity and superior mean pore size and has an effective influence on permeability [14]. Figure 2 c explains the GDLSP type of porosity, where SLM processed honeycomb lattice structures with a wall thickness of 100 μm of different pore sizes. It is observed that blue curve peaks at around 15 μm area and 200 μm. Fifteen micrometers is not the intended porosity, but generated due to insufficient laser energy [13]. Another GDLSP-type porosity of 1-mm targeted pore size in three different lattice designs (triangle, hexagonal, and rectangular) was processed through SLM technology, as shown in Fig. 2 d. Based on the information, it can be easily concluded that GUP delivers a lower pore size and porosity compared
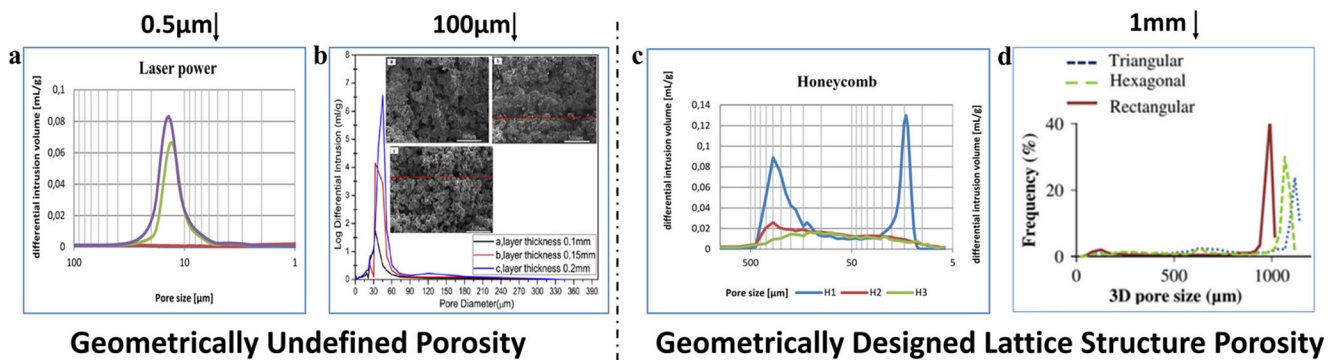
Fig. 2 **a**, **c** SLM process parameter (laser power)–optimized pore size [13]. **b** SLS process parameter (different layer thickness) pore [14]. **d** SLM-processed triangle, hexagonal, and rectangular lattice designs, with pore size around 1 mm [15]

with GDLSP; however, selecting the type of porosity depends on the intended application [15].

2.1 Geometrically defined lattice structure porosity

Even though AM is capable of building structures in any shape, the underlying quality of the 3D object may directly depend on the design and fabrication parameters. Conventional manufactured porous parts typically consist of a huge number of randomly shaped pores in various sizes/shapes. However, biomedical application and some categories of filtration applications require a defined pore shape and size. So, particularly, this kind of applications uses GDLSP type of porosity for the desired pore size, shape, porosity, and permeability in AM parts [2]. In GDLSP design, structural elements, either point lattice units or polyhedral lattice, are arranged recurrently to obtain a porous structure. The required structural unit cells are designed by computer-aided design, ISP (implicit surface modeling), IBD (image-based design), and topology optimization technique [6].

Depending on manufacturability considerations of definite AM technologies and 3D geometry properties, Chua et al. have attempted to design a standard library digital model containing 11 types (*cube, cuboctahedron, truncated octahedron, truncated cube, rhombicuboctahedron, truncated cuboctahedron, triangular prism, rectangular prism, hexagonal prism, octagonal prism, and rhombic dodecahedron*) of unit cells. In this design model, every kind of polyhedrons was arranged recurrently in 3D space by connecting vertices or edges and linked at faces [16, 17]. Xiang et al. summarized the range of porous structures based on different kinds of unit cells such as periodic uniform unit cells, anisotropic unit cells, liner porosity gradient unit cells, and hybrid unit cells [6]. Alternatively, Jia et al. implemented a bottom-up method for building the 3D porous scaffold and developed a standard library known as "Computer-Aided System for Tissue Scaffolding (CASTS)." CASTS library system allows the user to choose from nearly 20 polyhedral shape unit cells and provide optimized limits to attain the desired pore size and shape

[18]. The optimized polyhedral units are repeated continuously in the 3D arrangement and form a shape that suits the intended application. Figure 3 a shows different polyhedral units as an example and their resulting chunks or blocks produced by using the CASTS scaffold library.

Figure 3 b explains the development methodology of 3D-printed object in three phases, namely, selecting unit cell topology, specifying porosity, and obtaining desired pore size through generating lattices by patterning identical unit cells. Using this system, Egan et al. initially selected the unit cell (lattice cell) topology from the standard unit cell library to shorten the multifaceted design space. As mentioned, topology selection is the initial point for changing the scaffold properties by optimizing the diameter of the beam and lattice cell length. Once selecting the unit cell topology, desired porosity is specified by defining the diameter of the beam to lattice cell length. This is the most crucial step in the entire process because the mechanical properties are remained fixed for a specified porosity irrespective of premeditated pore size. In design point of view, for a given porosity, the diameters of the beam and lattice cell length are tunable parameters to attain any pore size for a unit cell [19]. Lattice structure design was further divided into uniform porosity and gradient porosity lattice designs based on their specific application. Figure 4 shows porosity and different porous structures of SLM-fabricated Ti6Al4V (T64) material based on different types of unit cells. The reasons behind studying different unit structures in each type of unit structure has its own advantages. For instance, cubic-type unit cells in Fig. 4 a show a more fatigue life when compared with diamond [Fig. 4b] and truncated cuboctahedron [Fig. 4c] structures [20]. In the current article, establishing territories and discussing between two types of porosities have been placed in. But, discussing advantages and disadvantages of different lattice structure designs is beyond the scope of this paper.

Lijun et al. designed and fabricated functionally graded T64 alloy lattice structures [Fig. 5 a and b] by SLM technology and investigated the mechanical properties under a very low and high strain rate. It has been reported that the specific
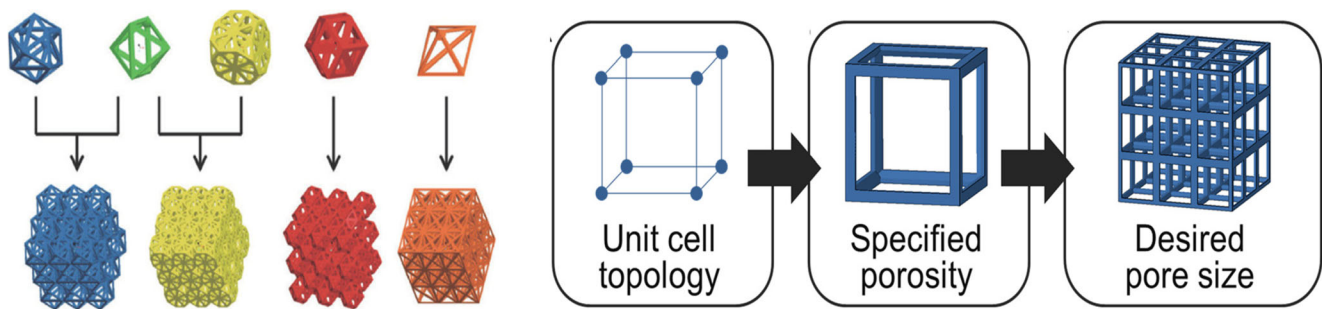
Fig. 3 **a** Examples for different types of polyhedral units [18]. **b** Lattice design for 3D printing of scaffold [19]

strength, specific energy, and collapse strength of SLM-classified lattice structures are much advanced than those of uniform structures [23]. Figure 5 c shows functionally gradient T64 alloy mesh structures made by electron beam melting (EBM) process. This mesh structure consists of three different pore sizes of ~ 600, ~ 400, and ~ 200 μm. Experiment results indicate substantial changes in the spreading of cell nuclei on different pore sizes [24]. Khoda et al. proposed a novel micronozzle extrusion–based AM technique to generate an interconnected and controllable heterogeneous architecture for tissue engineering applications. The proposed methodology tends to use a bi-layer pattern of radial and spiral layers to generate porous architecture with a functionally gradient porosity. With this reproducible technique, the 3D porous scaffold structure with controllable pore size and porosity can be achieved by stacking the designed layers consecutively layer by layer vertically. It is proposed that various critical properties for tissue engineering application such as continuous/interconnected variable porosity, pore size, structural integrity, oxygen diffusion during cell regeneration, cell differentiation, and guided tissue regeneration can be obtained with reproducible results [25]. Contuzzi et al. proposed a method of design for additive manufacturing (DfAM) to build metal random foam structures for lightweight metal structure fields. With

the desired fractional density and several other technical requirements of the foam, the geometry was optimized and an interconnected porous structure was generated using the proposed algorithm. The algorithm was further validated with a test print using laser powder bed fusion system [26].

A model and an overview of the material design selection procedure for each type of material (metals, ceramics, and polymers) depending on the porosity are depicted in Fig. 6.

2.2 Geometrically undefined porosity

In 3D printing, porous parts are achieved by different methodologies. Geometrically undefined porosity was achieved by controlling the process parameters of AM process. The following sections briefly discuss on process parameters of each type of AM process. In each process, technology has its own rewards and difficulties and the choice of which the user can have had been discussed in detail.

2.2.1 Inkjet 3D printing

Inkjet 3D printing is a solid freeform powder bed–based fabrication process developed by Massachusetts Institute of Technology in the early 1990s [27]. The key principle is that
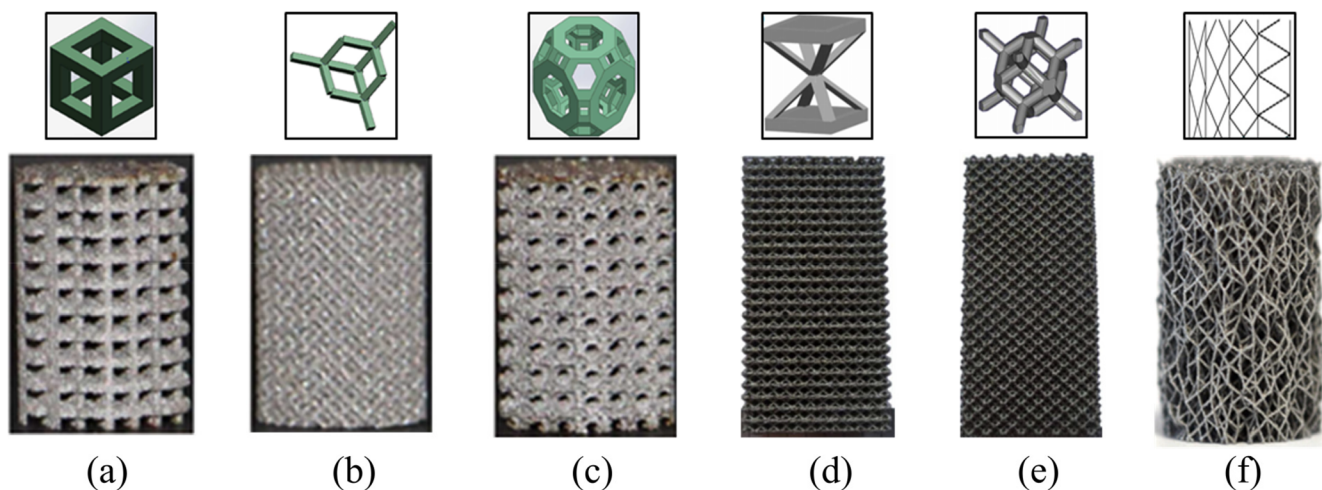

Fig. 4 Schematic drawings and images of different porous structures based on different types of unit cells used for manufacturing: **a** cubic [20]; **b** diamond [20]; **c** truncated cuboctahedron [20]; **d** G7 shape; **e** dodecahedron [21]; **f** stochastic structure [22]
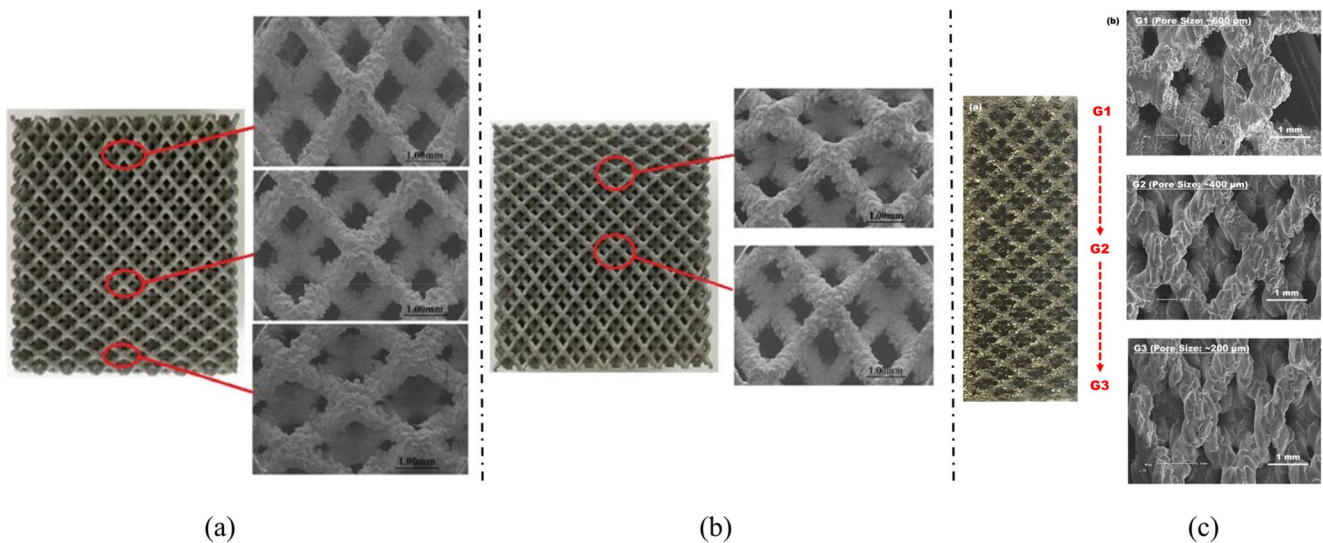
Fig. 5 Gradient porosity made by different processes and materials: **a** Ti alloy continuous gradient [23]; **b** Ti alloy stepwise gradient [23]; **c** Ti alloy gradient mesh structure [24]

a pre-designed 3D model is broken down into a series of 2D slices of a certain thickness. The 2D slices are created by selectively depositing the liquid droplets (binder or solvent) on powder bed by the ink print head to connect the powders layer by layer. After each printed layer, powder bed is lowered into pre-defined layer thickness and a new powder is deposited and leveled with rotating rollers for next layer printing. The finished object is a removed powder bed followed up by post-printing steps including de-binding and sintering processes. The complete layout of the inkjet 3D printing system is illustrated in Fig. 7. The lack of high-power/energy input is one of the main advantages of 3D printing/ink jet processes [28]. Feedstock material (mixing with binders, filler material, pore formers), printing with solvent jetting or binder jetting into desired shapes, curing the printed parts, de-powdering, de-binding, sintering, infiltration, annealing, and finishing were considered the crucial steps in inkjet 3D printing [29, 30] (Fig. 7).

Based on the binder location, the process can be classified as either (i) solvent jetting process or (ii) binder jetting process. In solvent jet process, binder materials are homogeneously mixed with feedstock material and the solvent is printed by print heads; subsequently, reaction occurs and was synthesized into other compounds. In binder jetting process, the binder material was selectively deposited in a liquid state by print heads on metal powders [29].

In 3D printing (3DP), porous parts were achieved by different methodologies such as:

1. Solvent jetting on feedstock material (a mixture of binder material and metal powder). The binder material acts as the porous or space holder after sintering [32, 33].

2. Binder jetting on powder feedstock. Powder size, shape, sintering time, and temperature (sintering profile) regulate the pore features and final porosity [34, 35].
3. By adding space fillers in liquid binder during binder jetting on powder bed method [29].
4. Mixing the fugitive material with metal powder in feedstock material and in binder jetting process. This fugitive material acts as the space holder during the build cycle and makes the porosity during sintering process by evaporating [34]

Porosity in inkjet-based 3D printing can be classified into macropores (pores by design) and micropores (pores by the process). These micropores were again classified into larger micropores generated by burning of the binders in the de-binding process and smaller micropores arising from leftovers of packing gaps between metal particles after sintering process [29]. Various process parameters can contribute to making the porous parts with binder jetting process. Powder shape, layer thickness during binding, part direction in bed, power output, roller speed and feed-to-powder ratio, and ink saturation level are the important parameters to be considered during part printing. It is important to note that interconnected porosity decreases with increasing printing saturation level (the percentage of the powder void space that is filled with printed binder) [34, 36] and minimization of layer thickness reduces porosity.

Zhang et al. explained the effect of the build orientation on porosity in 3D-printed alumina/glass composite parts and proved in his study that Y-axis build samples show a lower porosity compared with X-axis- and Z-axis-oriented build samples. There has also been some evidence reporting about X-axis-
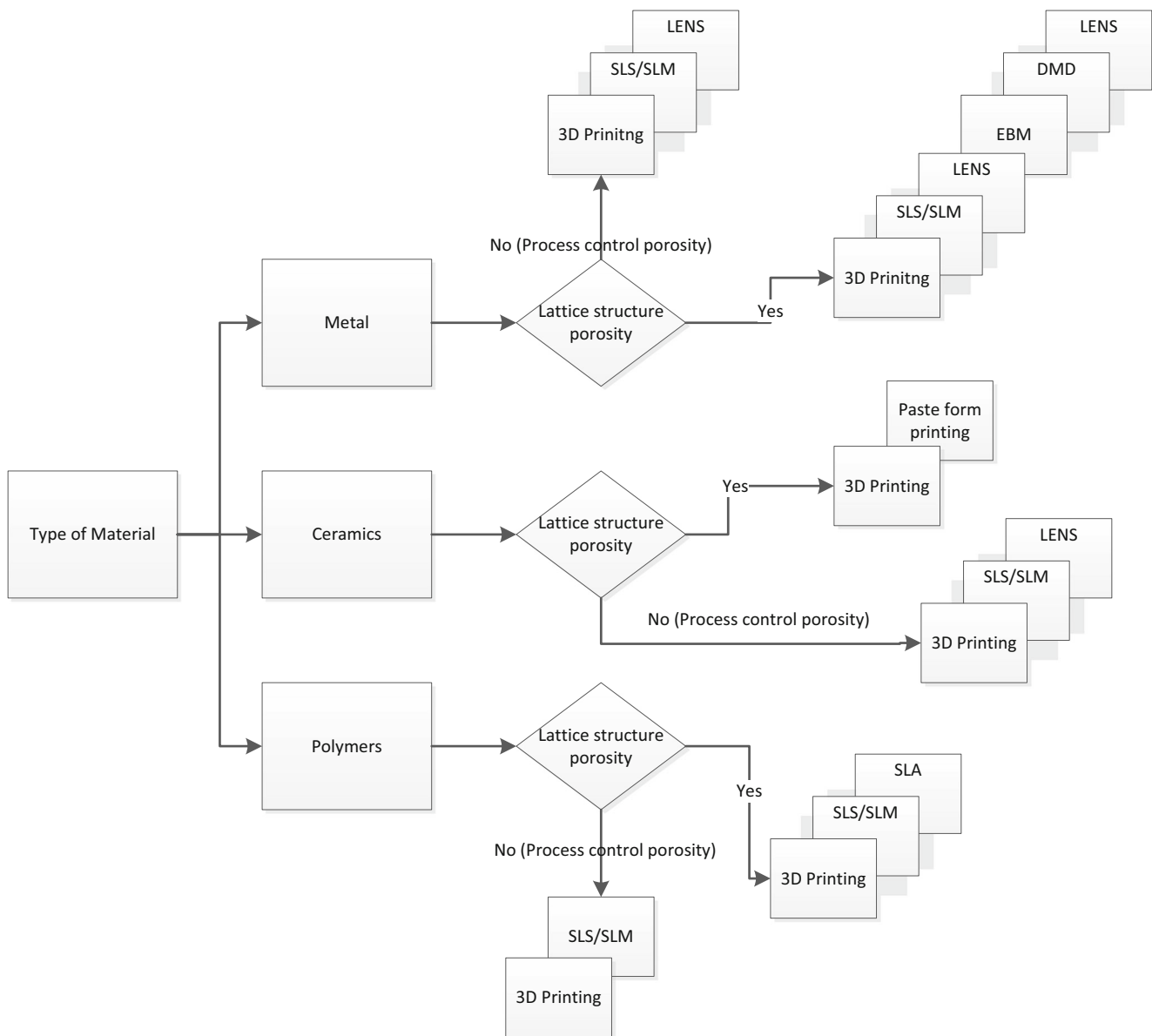
Fig. 6 Model for selecting AM process for metals, ceramics, and polymers based on the type of porosity needed

oriented print parts which are more porous than *Y*-axis- and *Z*-axis-oriented printed parts [37]. Eydivand and his team reported that *X*-axis-oriented print parts have more porosity than *Y*-axis- and *Z*-axis-oriented calcium sulfate–based scaffold prototypes. This trend is clarified by the development of constant strips along the *Y*-axis, whereas layers throughout the length of *X*-axis are crowded by these strips and finally being joined to each other. Down the *Z*-axis, single layers are laminated and exhibit interfaces and discontinuous porosity [38]. Sometimes, delay times/drying times between the ink deposition into a layer and the start of spreading the next layer of powder also induce porosity into the sample. Farzadi et al. reported the drying time or delay time effect on porosity when there is a longer delay/drying time; binder effectively penetrates and wets both horizontal and

vertical directions over the powder surface. It results in fewer empty spaces among the powder particles and makes fewer voids and micropores [38, 39]. Miguel et al. studied the relationship between the interconnected porosity and printing saturation level of calcium phosphate 3D-printed samples. It has been reported that interconnected porosity decreases with increasing printing saturation level (the percentage of the powder void space that is filled with printed binder) [36]. Power control/heater power corresponds to the heating rate and temperature of the part being made, and these parameters directly control the drying time. De-binding and sintering processes (curing temperature/time, sintering time/temperature/atmosphere) are some of the important parameters for controlling and obtaining appropriate porosity in the 3D part [40]. In a nutshell, a higher
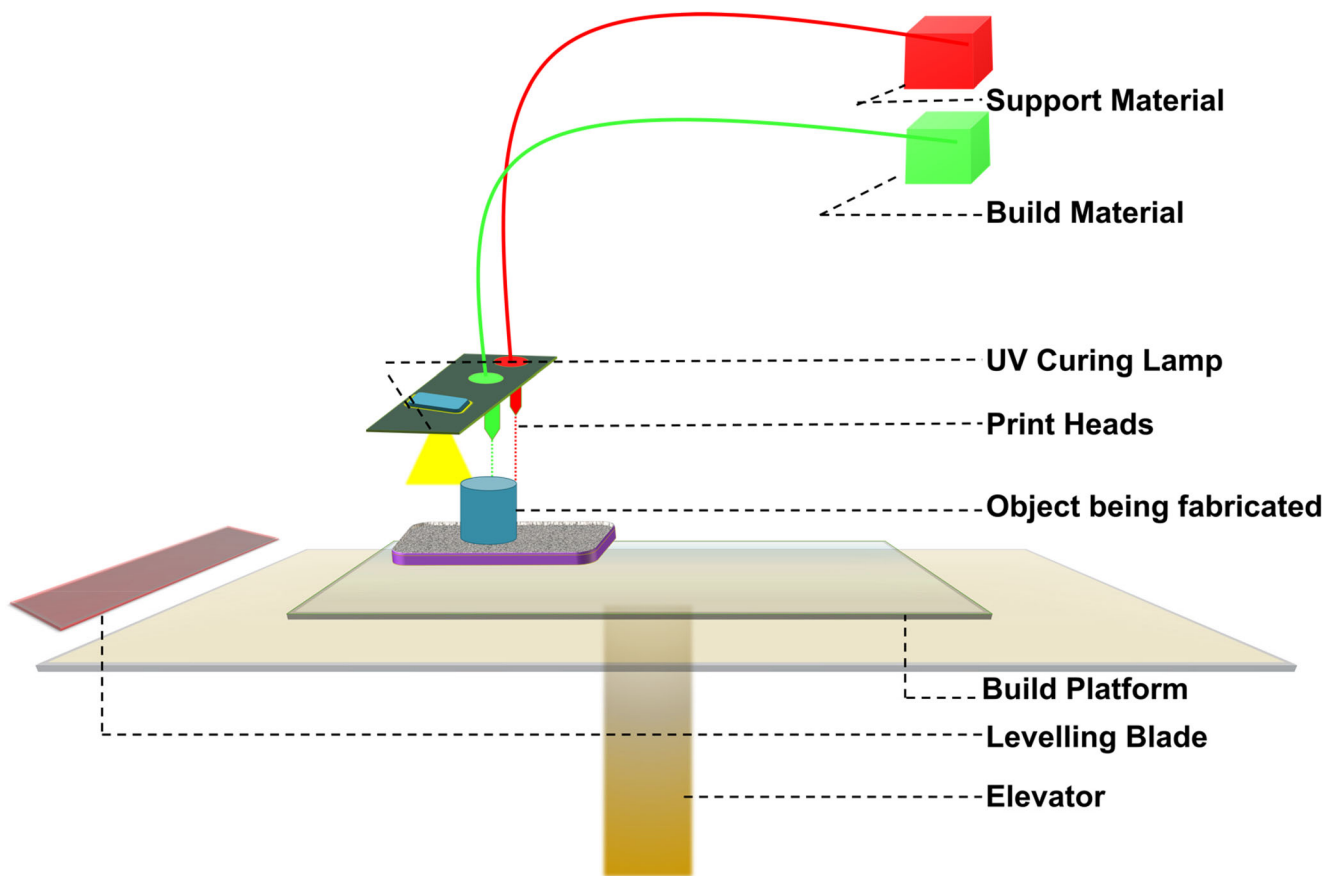
Fig. 7 A schematic of inkjet 3D printing [31]

sintering temperature is crucial to obtain open porosity and higher density. Lower particle size and spherical shape powders give a higher final density and lower porosity [30, 40].

Figure 8 shows SEM images of GUP type of porosity of different materials made by 3D printing (binder jetting) process. The images show a porosity range between 5 and 200 μm, i.e., polyethylene with a pore size of 100 to 200 μm (Fig. 8a) [41], 316L with 33% Nylon-printed sample with an undefined porosity (Fig. 8b) [34], metal composite (Fe-Mn-Ca) with a pore size of 5 to 30 μm (Fig. 8c) [42], and finally hydroxyapatite ceramic material with a pore size of 10 to 30 μm [43].

2.2.2 Selective laser sintering/melting

Depending on the nature of the powder fusion process, selective laser sintering (SLS), SLM, and EBM are three kinds of process capable of processing a wide range of materials to generate porosity. SLS and SLM processes are carried out in the inert gas atmosphere (argon or nitrogen) with a pre-defined laser power beam. This laser beam scans at a controlled speed on powder bed in selected locations as depicted in Fig. 9. Due to this laser, powder in the powder bed fuses into the solid material by either partial melting in SLS or full melting in SLM [44, 45]. In each process, the powder bed is pre-heated

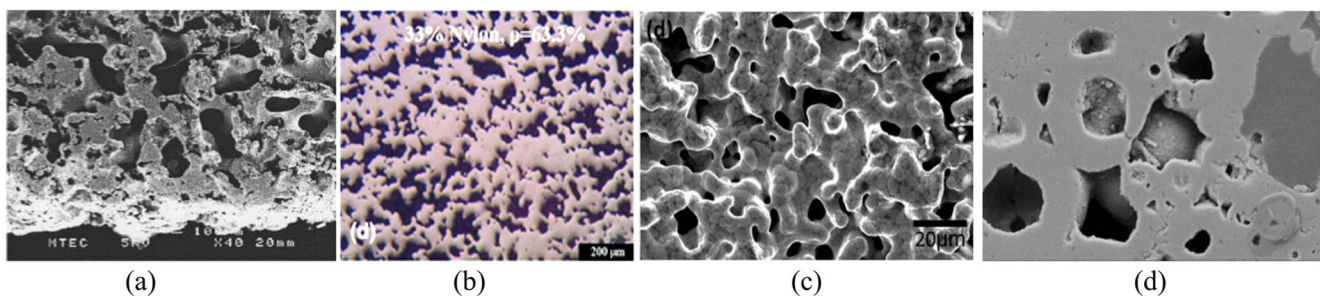| | | | |
| (a) | (b) | (c) | (d) |

Fig. 8 SEM images of 3D-printed GUP of different materials: **a** polyethylene [41]; **b** 316L with 33% Nylon [34]; **c** metal composite (Fe-Mn-Ca) [42]; **d** Ceramic (hydroxyapatite) [43]
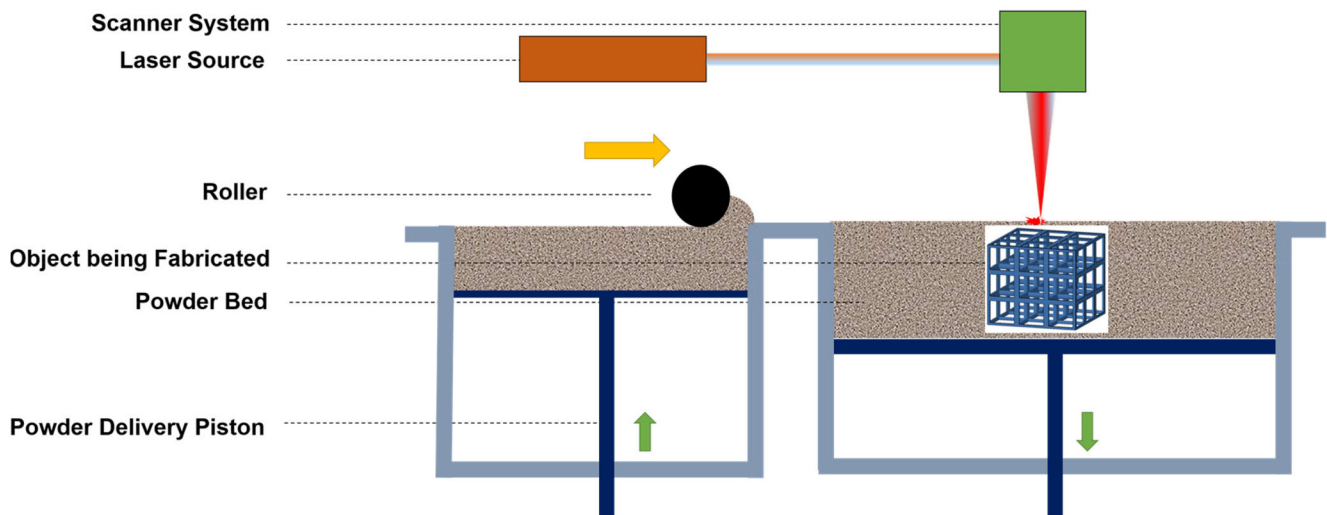
Fig. 9 Schematic of the SLM/SLS process: the part being built is immersed in the photopolymer resin and the part is fabricated layer by layer (image reproduced from [31])

close to the melting point of the material to reduce the thermal distortions and enable fusion in the preceding layer. After each printed layer, powder bed is lowered into pre-defined layer thickness and a new powder is deposited and leveled with rotating rollers, a wiper or doctor blade for next layer printing. The process is repeated until a printed part or object is completed and the printed object is removed from the supporting body [46]. SLS process is further classified into (i) direct laser sintering process (DSLS) and (ii) indirect laser sintering process (IDSLS). In IDSLS, metallic powder is initially coated with a polymer binder followed by sintering of polymer layer with laser beam. The metal powder grains are unaffected in IDSLS but require further thermal treatment for improving the density and reducing the porosity. In DSLS, there is no bonder or polymer mixed with metal powder and the process uses high-power laser beam applied for sintering [44, 47].

In the SLS method, hatch distance, part bed temperature, layer thickness, and laser energy density are considered some of the main contributors for obtaining part density or porosity. Faster laser scan speed in SLS process transfers lower energy to the materials that lead to more porosity in the sample due to less sintering. On the other hand, the higher layer thickness can lead to open porosity [48]. Savalani et al. have studied the effect of layer thickness on porosity by using hydroxyapatite (HA)-polyamide composites with HA content 58 wt%. The increase of pore size is attributed to the reduced specific heat capacity. Thicker layer thickness leads to weaker bonding between layers and increases the porosity of parts and vice versa [49]. In addition to specific heat and layer thickness, hatch distance is another important factor that controls part density or porosity. It can be explained that higher hatch distance can lead to the porous structure. As an example, if the laser beam spot size is 2 to 4 times larger than hatch distance, in other words, parts processed by hatch distance less than the spot size (25% or 50% less than spot size), a major part of the laser spot

may scan again previously scanned line, which leads to inter-line bonding and reduction in porosity. The case of hatch distance is the same as the laser spot size; overlapping does not take place, resulting in more porous part [48]. Tontowi et al. have studied the effect of powder bed temperature on density of SLS-printed parts of commercially supplied powders, Nylon 12 and glass-filled Nylon 11. The authors mentioned that the sintered part density is directly proportional to the temperature at a contestant laser power density. Increasing the powder bed temperature from 714 to 182 °C increases the SLS-printed part density [50]

Geometrically complex filters with customized shapes were 3D-printed by SLM to improve filtration performance by decreasing airflow resistance (back pressure) [51]. Spierings et al. studied the significance of process parameters (laser power, scan speed, and layer thickness) on porosity and reported a maximum porosity of 26% is achieved for stainless steel 17-4 PH/AISI 630 material [52]. Eberhard et al. analyzed the effect of hatch distance along with laser power/scan speed to achieve a maximum porosity of 17.35% for stainless steel 17-4H material. Based on the design of experiments (DoE), the authors have analyzed the influence of SLM parameters such as layer thickness, laser power, laser scanning speed, scanning path strategy, hatching space, laser spot size, and particle shape and size on porosity aspects of thin walls [53, 54]. Interestingly, the authors have calculated the impact of area energy density on porosity. Based on these parameters included in energy calculations, the energy density is expressed in terms of volume energy density, area energy density, and linear energy density. In linear energy calculations, the scan speed and the laser power are included, whereas in area energy calculations, an additional parameter (hatch distance) is included and in volume energy calculations apart from hatch distance, layer thickness, laser power, and scan speed were also added. This volume energy density is defined as

$$E_V = \frac{P}{V_s \cdot h \cdot S}$$

where E_V is volume energy density, V_s is scan speed, P is laser power, S is layer thickness, and h is hatch distance [13]. Lower laser power, high scan speed, high hatching distance, and layer thickness decrease the amount of energy transmitted, leading to a lower heat and partial melting of the metal powder and subsequently leading to the building of a porous structure. According to Eberhard et al., a study in the SLM process proved that increasing hatch distance and scan speed increases the porosity, followed by the interaction of both hatch distance and scan speed. According to studies, the areal energy density is a combined value that predicts the porosity for the SLM process [53].

2.2.3 Electron beam melting

Electron beam melting (EBM) is a powder bed fusion AM technique where the electron beam is used to selectively fuse powder layer in a vacuum chamber. This process is very similar to the SLM process except for energy source and vacuum build chamber [55]. In EBM, each layer is scanned in two stages, the first stage involves preheating the powder around 0.4 to 0.6 T_m followed by melting and fusing the metal powder. Dehoff et al. studied the influence of EBM processing parameters on engineering porosity in Inconel 718. It has been found that increasing the beam current and decreasing the beam pulse rate increase the porosity. Also, it has been reported that interconnected porosity is not obtained on EBM by controlling the abovementioned parameters [38]. After carefully reviewing the available literature, it is understood that porosity of EBM-made parts is mainly controlled by lattice design (GDLSP type of porosity) rather than process parameters. To our knowledge, a very limited work has been reported on GUP type of porosity using EBM technology.

2.3 Laser Engineered Net Shaping

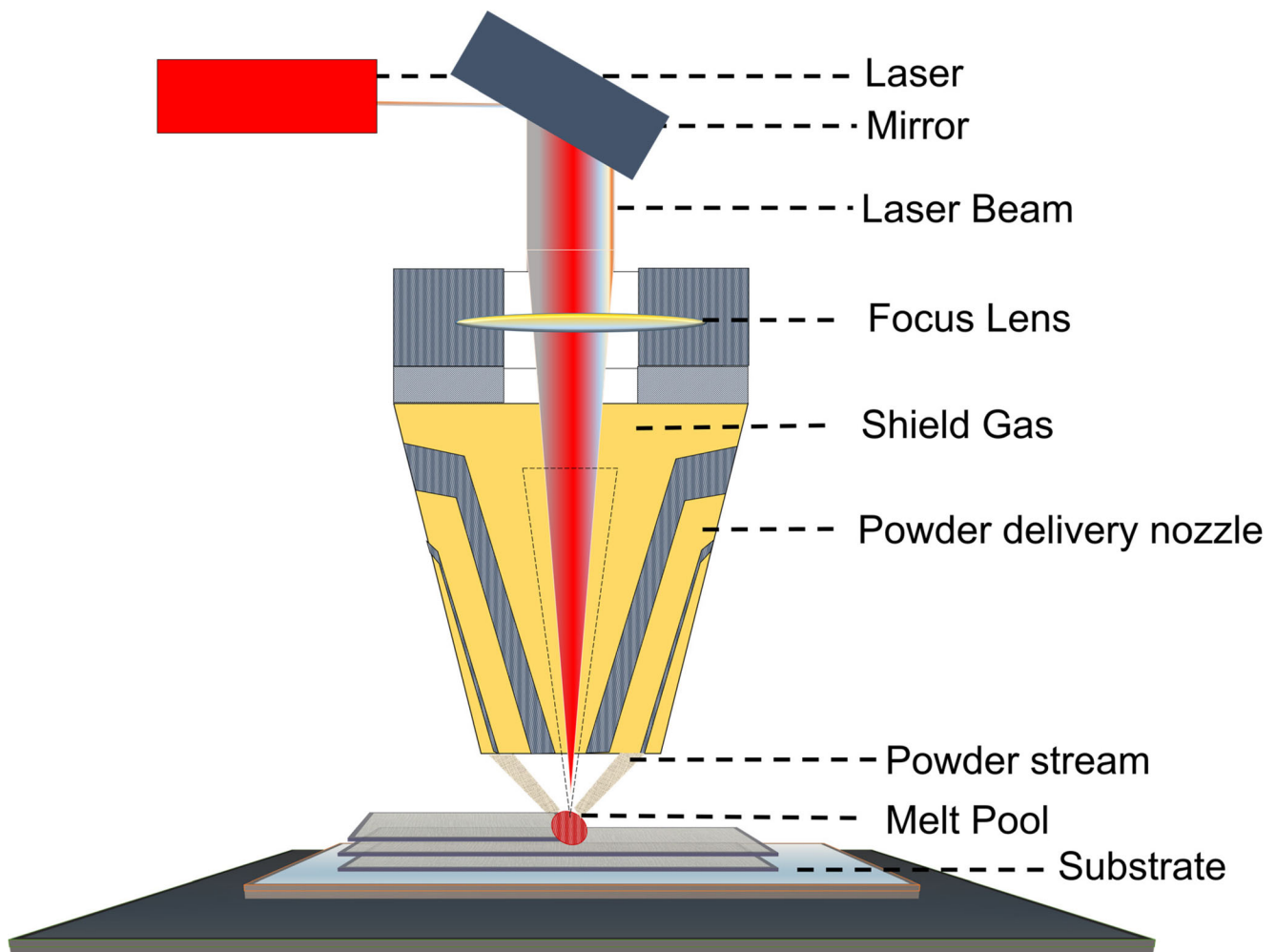Laser Engineered Net Shaping (LENS) [Fig. 10] is another well-known AM technique to construct near net–shaped

Fig. 10 Schematic illustration of the LENS process

3D Printing

- ☐ Powder size & Shape
- ☐ Binder type
- ☐ Layer thickness
- ☐ Printing saturation level
- ☐ Orientation
- ☐ Drying time / Delay time
- ☐ Heater power
- ☐ Sintering temperature
- ☐ Sintering time

SLS/SLM

- ☐ Volume Energy density
- ☐ Laser Power
- ☐ Scan speed
- ☐ Layer thickness
- ☐ Hatch distance
- ☐ Sintering temp
- ☐ Sintering time

LENS

- ☐ Feed rate
- ☐ Hatch distance
- ☐ Laser power
- ☐ Scan speed

EBM
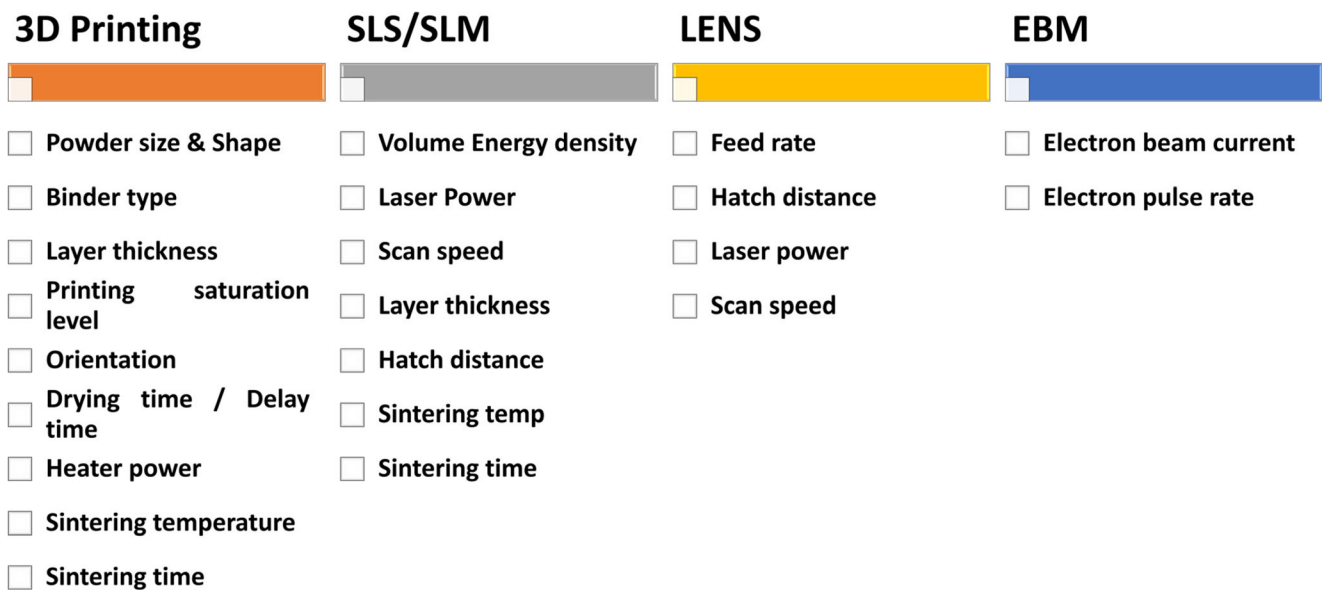
- ☐ Electron beam current
- ☐ Electron pulse rate

Fig. 11 Process parameters that control the porosity in AM process

metallic parts with multipart geometries without using any powder bed [56].

Mitun et al. studied the relative density/porosity of Ti samples controlling the LENS process parameters and observed hatch distance, laser power, scan speed, and feed rate are the foremost significant factors to control the porosity. The authors reported that increasing the powder feed rate or decreasing the laser power creates the partial porosity than the molten powder. Also, increasing the hatch distance induced a higher porosity into the sample mainly due to least overlapping of deposited metals. When laser power and powder feed rate are kept constant, melting of the metal powder depends on laser scan speed. With an increasing laser scan speed, interaction between powder and laser is reduced which leads to incomplete melting of powder, so that porosity increases [57]. Similar results were also observed by Felix et al. for their studies on CoCrMo alloy. The authors reported porosity increases with decreasing laser power, increasing powder feed rate, and increasing scan speed [58]. Figure 11 provided information about all the AM process parameters that control the porosity in AM process.

3 Additive-manufactured porous material applications

Conventional manufacturing processes for porous applications have limitations on design flexibility, cost of tooling, lead time delivery, manufacturability, etc. AM has now almost considered a better alternative for porous applications and been adapted by many industries progressively [59]. Considerable research is being carried out in many disciplines such as engineering (filtration and purification,

plastic injection molds, heat exchangers/heat pipes), energy (batteries and electrodes), medicine (dental, orthopedic, pharmaceutical), health care (medical devices), and food and chemical industries to exploit the advantages of AM [14, 51, 60–68]. A summary of applications of 3D printing is contained in Figs. 12 and 13.

3.1 Engineering applications

3.1.1 Filtration, purification, and membrane applications

Manufacturing of complex filters using traditional manufacturing techniques is highly difficult but can be easily manufactured by using AM technologies to high precision. Applying AM technologies to filtration and membrane fields is relatively new, and a very little progress has been made in this arena. For the first time, Yadroitsev et al. and his coworkers studied the filter flow resistance/back pressure and filtration performance of filters made by the SLM process for chemical and biomedical applications. Thin fine–walled 3D filters made from stainless steel (grades 316L and 904L) were evaluated to optimize SLM process parameters to produce a material with open pore structure. Also, functionally graded porous filters were synthesized with nickel alloy with polycarbonate. It has been observed that permeability and pressure drop strongly depends on synthesis parameters [51].

Croft Additive Manufacturing (CAM) is a UK leading company actively working on applying AM in filtration field. CAM mainly focuses on using SLM to make stainless steel 316L metal filters to remove contaminants in compressed air [73]. Burns et al. suggested the SLM printed wedge wire metal filter components have offered a higher flow rate at a very low pressure drop [74]. The
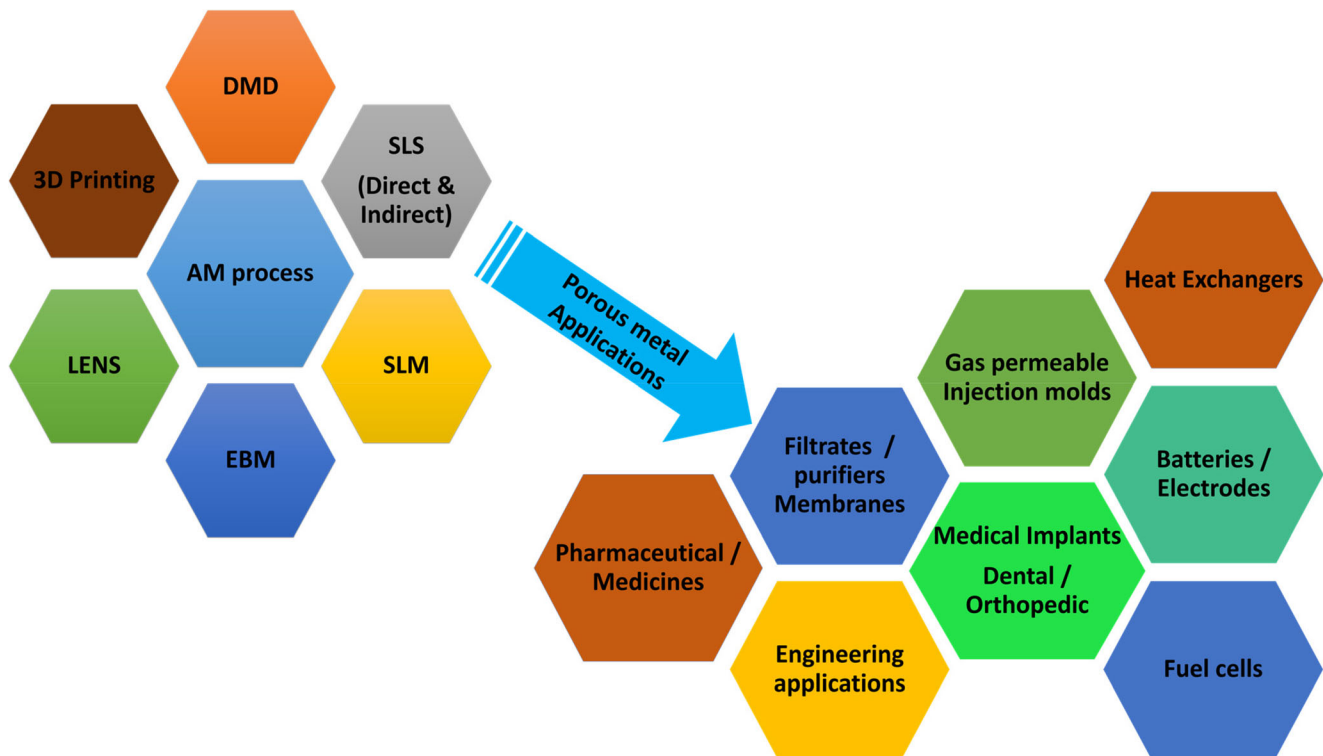
Fig. 12 AM process for various porous applications

same research group reported designing of 316L 3D filters with a powder particle size ranging from 10 to 45 μm and achieved a layer thickness of 50 μm. These filter meshes, such as filter holes in-line with filters, decrease the end users' energy requirements by at least 15% in fluid pumping sectors [75]. Mengxue and his team proposed and studied a novel method by combining the SLS and particulate leaching for making hierarchical 3D-printed porous Nylon filters for high permeable water purification. The authors studied the effect of different laser energy densities and layer thickness to control the graded porosity by using NaCl as pore-forming agent. The porosity decreased with increasing laser energy density, and samples made with larger layer thickness show a higher pore size and high porosity. Filtration test results show filtration efficiency was increased by 95% for the suspension containing particles with size distribution in the range of 15 μm–120 μm, and the filtering precision was about 17.6 μm filtering precision for 15 to 120 μm sized particles suspended in filtration medium [14]. In another study, Ryan et al. and his co-workers worked on additively manufactured Inconel 718 metal porous discs for separation of helium gas from liquid natural gas. Two different approaches were adapted to manufacture porous Inconel 718 metal membranes. One method is to optimize the EBM process parameters (beam current and pulse time), and another one is by using four different mesh

structures by varying the strut thickness to control the porosity. The authors have used three different methods to measure the porosity, and particularly, image process technique porosity measurement method showed a maximum porosity (~ 30%) in membranes in those parts made by varying EBM process parameters [76, 77]. Low et al. reviewed the applications of 3D printing for membrane fabrication. The article provided a brief illustration and screening methodology for selecting AM technique for membrane fabrication based on printing resolution, accuracy, build size, speed, printed materials, and mechanical properties. While it is mentioned that current AM technologies are not progressed for nanofiltration, however, they can able to print dense membranes with pore size more than ~ 100 nm [78].

3.1.2 Plastic injection molding molds

Kojima et al. proposed the construction of gas permeable molds for reducing process-related defects such as short shots and gas burning. Gas permeable molds were created with metal laser sintering and high-speed milling and controlled the porous structure by optimizing the laser sintering process parameters. The experimental details demonstrated that the AM-manufactured porous molds were able to reduce the mold defects and help to lower the injection mold pressure [60]. In another study,

Fig. 13 Next generation of application of porous materials using AM technologies: **a** 3D printing of interdigitated Li-ion microbattery architectures [69]; **b** 3D-printed components of microbial fuel cells [70]; **c** hybrid mold inserts [image credit: FADO group]; **d** heat exchangers [image credit: EOS Mfg]; **f** novel filter designs [71]; **g** 3D-printed orthopedic [image credit: DiSanto, Inc.] and dental implants [72]

Narahara et al. studied the similar application (permeable molds) with lattice pore structure created by laser sintering combined with high-speed milling and reported the reduction in mold defects [61]. Klahn et al. reported

the assembly of pneumatic ejector system (porous mold inserts) by laser AM which uses the air to eject the molded part from mold cavity instead of metal pin ejectors [79].

3.1.3 Heat pipes

Porous structures have a capacity to retain low surface tension liquids against an involuntary pressure difference. Porosity is considered a crucial parameter especially in 2-phase equipment such as heat pipes by offering the capillary pressure for driving the 2-phase circulation. The porosity is also capable of providing the flow path by acting as bridges from one end to another and helps working liquid to flow easily inside the heat pipes. 3D-printed porous materials are now extensively used in thermal management systems. Jafari et al. investigated the thermal conductivity of different liquids from SLM-made stainless steel 316L porous structure and concluded the possibility of using AM for heat pipe technologies [62]. Ameli et al. developed and studied porosity and the permeability of SLM 3D-printed aluminum/ammonia porous wick heat pipes with different pore diameters ranging from 300, 500, and 700 μm cubic units. The authors observed the negligible change in permeability from 10^{-10} m^2 for 500-μm unit cell samples to 10^{-13} m^2 for 300 μm. A maximum porosity of 58% has been achieved for 500-μm regular lattice pore structure [63]. Only limited literature is made available on using AM for heat pipes.

3.2 Energy applications

3.2.1 Fuel cells

Fuel cells, the oldest energy conversion technology, are high-energy efficient devices that work on the principle of transforming chemical potential energy (electrochemical reaction) directly into electrical energy and heat. Guha et al. applied the binder jetting process to fabricate solid oxide fuel cell (SOFC) components such as anode, cathode, and oxygen ion–conducting electrolyte for high-temperature applications. Ni-YSZ (nickel oxide-yttria-stabilized zirconia), lanthanum strontium manganite, and YSZ powder materials were used to fabricate anode, cathode, and electrolyte respectively. It is demonstrated that 3D-printed fuel cell withstands at higher temperature application (750 °C) with consistency voltage current performance [80]. Inkjet printing is one of the matured AM processes for the fabrication of electrodes for electrochemical reactor, i.e., for solid oxide fuel cells (SOFCs). Yashiro et al. successfully reported the fabrication of the desired pattern of cathode layers by depositing dots through inkjet printing. Rheological properties of the ink, amount of ink ejection, solid loading, platen temperature, number of passes, and pore formers are critical parameters to achieve the require thickness, microstructure, and porosity [65].

Recently, AM techniques have been explored to fabricate devices to host microorganisms for powering home-based devices, famously known as microbial fuel cells (MFCs) [81]. In MFCs, microorganisms act as a biocatalyst and convert the energy stored in biodegradable organic/inorganic compounds into bioelectricity. In these batteries, anodes conduct electrons as well as host and carry the bacteria. Anodes with porous structure are crucial for providing a high surface area, high conductivity, and biocompatibility. Calignano et al. proposed the use of AM technologies for bioelectrochemical systems and made the cylindrical-shaped MFC cell anodes with aluminum alloy using the SLM process. These anodes are made with lattice structure and with a mean theoretical diameter of 0.85 mm. The experiments proved that the energy recovery close to 3 kWh m^{-3} per day has been achieved by electrodes and energy production is greater than metal anodes [64]. Bian et al. explored power generation enhancement of MFCs using 3D-printed porous carbon anodes. Open porous 3D-printed carbonaceous (3D-PCP) anodes were fabricated by a combination of DLP using UV curable resins and precise control of carbonization process in a tube furnace. The 300-μm porous carbon anodes, i.e., 3D-PCP anodes, significantly boosted power density (~ 238.4%) and generated a maximum voltage (453.4 ± 6.5 mV) when compared with pure carbon cloth anodes (188.5 ± 2.7 mV). The superior performance of MFC power generation is being attributed to the secondary porous surface [82]. Tang et al. reported the application and fabrication of 3D printing anodes in urine-powered MFCs. The 1.5-mm pore size anodes using X-shaped lattice structure were designed using 3DP technology for interconnected porosity and applied polyaniline (PANI) on electrode surface for biocompatibility improvement. An electropolymerization process is used as a surface modification technique for improving 3D-printed anode performance. 316L stainless steel (316LSS), Ti6Al4V (Ti64) alloy, and its surface-modified samples were used for performance evaluation, and results show that PANI-coated 3DP-SS electrode showed lowest activation resistance (less than 15 Ω) and highest maximum power density (0.934 W m^{-3}). Due to high porosity, the surface-coated 3DP-printed macroporous MFC anodes were not made to clog easily and can be a promising application in microbial electrochemical systems [83].

3.2.2 Batteries and supercapacitors

Electrochemical energy systems such as batteries and supercapacitors composed of electrodes and electrolytes have been studied widely owing to their high energy density efficiency and long cycling performance. Inkjet printing and direct ink writing are two famous AM techniques for creating 3D objects much below room temperature for energy device system applications [84].

Delannoy et al. applied the AM technology inkjet printing to make porous LiFePO$_4$ (LFP) electrodes for microbattery applications. The authors successfully formulated ink with the LiFePO$_4$-positive electrode by combining the carbon

block as a conductive additive and polyacrylic-co-maleic acid (PAMA) as a dispersant and binder. The formulated 3D-printed thin electrode of 85 wt% of LiFePO$_4$, 10 wt% of carbon black and 5 wt% of PMMA achieved 65 to 70% of porosity and demonstrated a very high rate charge/discharge performance of 80 to 70 mAh g^{-1} [66]. In a similar kind of study, Changyong et al. [67] studied the low-temperature direct writing (LTDW)–based AM technique to manufacture 3D LFP porous electrodes for the first time. Using LTDW, high porosity (71.8%) in electrodes is achieved when compared with room temperature direct-writing process (61.4%). Initially, LEP ink was printed layer by layer in a very low-temperature chamber, and printed electrodes were made to freeze to sustain the mechanical properties and the configuration of the printed topographies. To obtain the 3D porous electrode, the electrode is further freeze-dried in constrained chambers. Liu et al. applied a combination of DMLS and co-electrodeposition method for fabrication of pseudo capacitors. 3D hierarchical porous metallic scaffolds fabricated from 316L stainless steel were printed for hosting higher quantities of active materials like MnO$_2$, Mn$_2$O$_3$, and poly[3,4-ethylenedioxythiophene]. Poly[3,4-ethylenedioxythiophene] polymer was able to deposit by co-electrodeposition to act as an adequate binder to enhance the conduciveness and capacitance of MnO$_x$. Porous scaffold hosting active material exhibits a higher areal capacitance, lower resistance, and better cycling (reduction and oxidation) capacity than the dense electrode. In addition to this, 3D-printed porous structure avoided the delamination of active material [85].

Azhari et al. applied the powder bed binder jetting process to make thick porous thermally reduced graphene oxide (TRGO) electrodes for high-performance supercapacitors. The authors hypothesized that interconnected pore structure allows rapid ion transportation inside the electrodes of electrochemical devices such as supercapacitors and batteries. Thick supercapacitor electrodes of 300 μm thickness with 12-mm-diameter electrodes were impregnated with palladium (Pd) nanoparticles for improving electrode performance and decreasing the contact resistance between powder agglomerates. This work demonstrated highest gravimetric capacitance of 260 F/g and areal capacitance of 700 mF/cm^2 till date compared with any other graphene-based porous structure electrodes [86].

3.3 Medical implants/tissue engineering

3.3.1 Medical implants (dental and orthopedic)

In the field of medicine, AM has significantly improved the ability to prepare structures with precise geometries, permitting the production of patient-specific implants involving complex surgeries. Human skeletons contain two types of bones; one is trabecular bone and another one is cortical (compact) bone. Each type required a different degree of porosity and association. Compact bone porosity is 3 to 5% and trabecular bone porosity is up to 90% [68]. For an implant to qualify medically, it needs to have a good biocompatibility and appropriate pore size, porosity, and mechanical properties. Microporosity is a crucial element for osteoinduction; open porosity is important for osteoinduction, osteoconduction, and osteointegration. Current average pore size for orthopedic applications is desired up to 400 to 600 μm with volume porosity of 75–85%. Appropriate open pore size and interconnected pores, and the shape of the pores allow tissue ingrowth, cell attachment, and proliferation [45]. An appropriate balance between implant strength and porosity is required to ensure the scaffold can withstand the applied complex stress during surgical operation [87]. Most of the AM processes for 3D printing materials for orthopedic and dental applications are SLS, SLM, EBM, and LENS. Table 1 briefly summarizes the processes, materials, and achievable porosity with process parameters and lattice design structures.

To fix and support the lost teeth, dental implants were used as artificial tooth roots for more than five decades. But, commercially available implants provide very limited design options and sometimes can be a matter of question based on patient's oral conditions. As we know, dental tissue consists of enamel, dentine, cementum, and pulp. Open pores in dentin have the important function to connect the Tomes' fibers and exterior of odontoblasts sit within the teeth. Usually exposed/open porosity of dental tissue is in the range of 1.11 to 3.08% of its volume [92]. In dentistry, metallic metals such as titanium

Table 1 Details of metallic materials, processes, porous cell structures, and porosity for biomedical applications

Sl. no.	Material	Process	Porous cell structure	% of porosity	Strut thickness	Pore size	Ref
1	NiTi	SLM	Rhombo-dodecahedral unit cell	88	300	–	[88]
2	Ta	SLM	Dodecahedron unit cell	80	150 μm	500 μm	[89]
3	Ti-6Al-4V	SLM	Cube	63–87	1020–1413 μm	451–823 μm	[6, 90]
4	Ti-6Al-4V	SLM	Diamond	64–89	641–958 μm	240–564 μm	
5	Ti-6Al-4V	3DF		39–68		160–680 μm	[91]
6	Ti	3D printing		41–65		50–150 μm	[33]
7	CoCrMo	LENS		10–18			[58]

(Ti), 316LSS, and cobalt-chromium (CoCr) [SLS, DMLS, SLM]; ceramics such as alumina (Al_2O_3) and zirconia (Zr_2O_3) [SLS, stereolithography, inkjet]; and polymers such as polylactide, polycaprolactone, polyglycolide, and acrylic [stereolithography, fused deposition modeling] are extensively used to make dental implants by various 3D printing technologies mentioned [93]. One of the major material challenges in the dental application is the harsh chemical state in the mouth which leads to a higher corrosion. Ti and its alloys are widely accepted in dentistry in terms of dental implants because they are highly resistant to pitting corrosion during dental usage [93]. Traini et al. studied T64 alloy with the SLM process for gradient porosity from the inner core to the outer surface and reported that metal surface mean porosity is 28.7% [94]. From the study of the available literature, we can conclude that the applications of porous implants for orthopedics and dental are similar, with the only difference in the amount of porosity and pore size.

3.3.2 Pharmaceutical applications

Even though there is no porous metal AM for drug delivery devices, it is worthwhile to mentioned porous polymer application in pharmaceutical applications. AM in pharmaceutical drug delivery is a highly anticipated technology and may have a tremendous impact in the area of personalized medicines in the coming future. Cheah et al. explored the use of the SLS process to make polymeric drug delivery devices with a dense porous core wall for drug storage and release. In their study, the authors optimized the laser power and scanning speed for obtaining required density, porosity, and porous morphology of drug delivery product. Polyamide (PA) is used as the building material and methylene blue was used as a drug model in place of an actual drug and it was concluded that drug delivery devices with different releasing profiles are successfully made

by the SLS process [95]. Fabrizio et al. studied the impact of SLM process parameters for oral drug–loaded products. In this work, it has been demonstrated that immediate and modified drug release profiles can be achieved by optimizing the SLS process parameters without degrading the drug. Initially, 3D-printed tablets with two types of pharmaceutical grade polymers (Kollicoat IR and Eudragit L100-55) were loaded with paracetamol 5, 30, and 35%. Later 3% of Candurin gold sheen was added to aid the sintering process of these polymers. Open and closed porosity was achieved to assist immediate and modified drug release by optimizing the internal chamber temperature and laser scan speed [96].

4 Porosity characterization

As we know, porosity is defined as a measure of the fluid storage capacity of porous material and permeability is the ability of porous media to allow the passage of fluid (liquid and gas). Porous materials have a high internal surface area that can be used to accomplish specific function or application. It should be noted that porosity is a geometrical property of the sample and consists of open, closed, and interconnected pores whereas permeability is considered a physical property of a porous sample [97]. Due to the influence of porosity in properties, a more in-depth analysis is essential before taking a prototype into the market. To assess the properties more quantitatively, multiple methods are made available to characterize pore structure, pore size, pore volume, and pore distribution. In AM, several types of porosity characterization methods were available for porosity characterization. However, only a few methods such as optical microscopy, scanning electron microscope (SEM), X-ray computed tomography (X-ray CT), Archimedes' method, and mercury porosimetry are some

Bulk density measurement	X-ray CT scan	Optical microscopy
•Total porosity can be measured •No information about closed or open porosity •No pore size information	•Total porosity can be measured •Information about open and close porosity •Pore size & shape above 1μm can be identified •Volume sensitive	•Provides prior information •Pore size & shape above 1μm •Surface sensitive

SEM	Mercury porosimetry
•Pore size & shape above 5nm can be seen visually •Surface sensitive •Rarely used for pore analysis	•Open porosity •Pore size can be measured •Volume sensitive •Pore size above 1.5nm can be identified •Easy measurement

Fig. 14 Advantages and disadvantages of various characterization techniques for porosity measurement

widely used characterization methods for AM parts. Herein in Fig. 14, we have summarized all characterization methods with their advantages and limitations.

Back in 2009, F42, an American Society for Testing and Material (ASTM) committee, initiated the development of a set of standards for AM to cover various aspects such as terminology, executive, strategic planning, design, materials, and process and test methods. In particular, subcommittee F42.01 reports the adaptive test methods and approved F2971-13 standards for typical practices for test specimens prepared by AM. Despite having a large database of standards, a lot of work still needs to be reported on different test methods and evaluating mechanical properties of material made by AM process. In 2011, the International Organization for Standardization (ISO) committee TC 261 was established for AM, and ISO/TC 261/WG3 subcommittee was formed to work on test methods [98].

4.1 Archimedes' method

Density/porosity of AM parts is generally measured by Archimedes' method. Standard ASTM B962-08 for standard test methods for measuring density of compacted or sintered powder metallurgy (PM) products using Archimedes' principle. Archimedes' method for finding the porosity or density of a material is calculated by the following equation:

$$\rho = \left(\frac{M_a}{M_a - M_w}\right)\rho_w$$

where M_a is the mass measured in the air, M_w is the mass measured in the water, and ρ_w is the density of water. Spierings et al. compared and studied density/porosity of SLM process–made 316L stainless steel parts of different densities (90 to 99.5% density) by using three different methods viz. Archimedes' method, x-ray analysis, and microscopic analysis. The authors concluded that Archimedes' method has showcased high repeatability, accuracy of measurements, and ease of usability of any geometry/part size among three methods for any given part densities. The use of acetone in Archimedes' method gives more accurate density measurement by reducing wall adhering air bubbles due to low surface tension of acetone [99]. Williams et al. used Archimedes' method for finding the porosity or density of an additive-manufactured part of maraging steel parts and observed that partially dissolved solvent in 3DP process shows a higher density and lower open porosity compared with the binder jetting process. The authors attributed relatively low density measurement to a poor powder bed density and insufficient deformation of spray-dried particles [100]. Similarly, Slotwinski et al. measured and analyzed porosity of CoCr samples made by the DMLS process and compared with

Archimedes', bulk/mass volume, and XRCT methods. All three methods generally agree with each other at lower porosity, but the Archimedes' method shows a lower value than the bulk/mass volume method for higher porosity samples. In higher porous samples, Water was infiltrated into the open pores that are open to the surface of 3D-printed part. It results in lower porosity values in Archimedes' method [101].

The main concern with "Archimedes' porosity measurement" is that occasionally, the results are flawed when the sample has an open porosity or cracks on the surface. Various successful attempts were adopted by sealing the open pores or cracks using a lacquer with a known density [66]. The main limitations of Archimedes' method are that it is not suitable for the materials which have closed porosity and it does not provide any information about the pore size and shape.

4.2 Bulk density measurement

Bulk density measurement is a direct measurement method for total porosity where basic mass and volume of the sample are measured to calculate the density of sample from the mass-volume relationship. This method gives average porosity of sample and not sensitive to localized porosity. Mass and volume measurements are very critical for accurate porosity measurement [101].

Total porosity equation is $\epsilon = 100\% \left(1 - \dfrac{\rho_{\text{sample}}}{\rho_{\text{standard}}}\right)$

where ϵ is total porosity, ρ_{sample} is density of test sample, and ρ_{standard} is standard sample density [13]. Stoffregen et al. used bulk density measurement to calculate the total porosity for GDLSP and GUP structures by making specific modification in SLM process. The maximum total porosity achieved by GUP is 36.02% and by GDLSP is 60% [13]. Manfredi and his team also used the same method to find the total porosity of DMLS-made Al alloy parts at different stages of part making and reported porosity values at different stages, i.e., 3.3% after DMLS process, 2.0% after shot peening, and finally 1.1% after polishing [102], whereas Paul et al. have used a similar method to study the Inconel 625 porous structures [103].

4.3 Mercury intrusion porosimetry

Identifying pore size distribution is critical for many aspects in a wide range of material applications and industries. Mercury intrusion porosimetry (MIP) is a nondestructive technique used in the calculation of porosity, pore size distribution, and pore volume for a wide range of powder particles. In this method, samples are impregnated with mercury at a gradually increasing pressure so that the mercury infiltrates into pores due to applied pressure. Pore sizes and pore volumes are

calculated by pressure-pore size correlation by tracking the amount of mercury infiltrated at each pressure [104]. MIP uses the Washburn equation to calculate pore size by assuming the shape of the pores is cylindrical.

Wash burn equation is $\Delta P = \gamma \left(\dfrac{1}{r_1} + \dfrac{1}{r_2} \right) = \dfrac{2\,\gamma\,cos\theta}{r_{pore}}$

where γ is surface tension of mercury, r_1 and r_2 are the curvatures of the interface, r_{pore} is pore size, and θ is contact angle between the mercury and solid

Jande and his co-workers characterized the uniform and graded porous polyamide structures made by SLS process. The authors have used the MIP method for measuring pore size distribution and measured the pore size which ranges between 5 and 100 μm, and the mean pore size is 20 μm by raising the pressure to a maximum value of 44 MPa [105]. It is observed and conveyed that pore sizes < 0.1 μm might be due to the failure of the specimens at higher infiltration pressures of mercury but do not truly represent the actual pore structure in the specimens. Abele et al. studied the influence of SLM process parameters on porosity and mechanical characteristics of stainless steel parts. MIP characterization technique is used to find out the average pore size and pore volume distribution and observed that pore size diameters are between 7 and 16 μm for energy densities below 1 J/mm^2. It is mentioned that above this specific energy, density pore diameters are not able to be determined because of closed pores and absence of open pores [53]. Using the same MIP method, Liu et al. compared the porosity of LTDW-printed electrodes with room temperature–printed electrodes and concluded that pore volume and porosity of LTDW are higher than room temperature–printed electrodes [67]. Verlee and his team studied the porosity control and density of SS 316L parts processed by the 3D printing process using different powder shapes and sizes and used MIP and bubble point test for pore size measurement. Based on the series of experiments, the

authors concluded that average pore size and permeability decrease with a fraction of open pore and particle size [35].

The major drawback of MIP is that this technique is not suitable for measuring the closed pore size. It will approximate the value of the interconnect pore sizes rather than the actual pore sizes. Quantification of actual inner pore size diameter is not possible by MIP as it measures the largest entrance diameter towards the pore. But any size between 500 μm and 3.5 nm of pore size can be measured using MIP [106].

4.4 Microscopy analysis

Microscopic analysis is a simple method of getting insights on surface topography, microstructure, pore distribution, surface voids, and cracks with any cross section of the sample. The low-magnification microscopic analysis is carried out using an optical microscope (OM), and the higher magnification (up to few thousand times) is carried out using scanning electron microscope (SEM). Carrying out optical microscopic and SEM analysis requires sample preparation such as cutting, epoxy potting, grinding, and polishing.

Figure 15 a shows SEM images of SLM-made GUP type of porosity samples made by changing the scanning speed from 1000 to 4000 mm/s and laser power from 100 to 400 W. From the images, it can be clearly understood that there is a direct proportional relation between porosity and scanning speed, i.e., increase in porosity while increasing the scanning speed. Also, at higher scanning speeds, a decrease in pore size can be observed with an increase in the interconnected porosity and total porosity. Figure 15 b shows microscopic, SEM, and μCT images of GDLSP-type porosity parts. SEM images clearly show the difference among the different lattice designs as well as pore diameters. Ramakrishnaiah et al. applied the SEM analysis for studying T64 dental implant microstructure and microporosity study. They observed uniform, completely
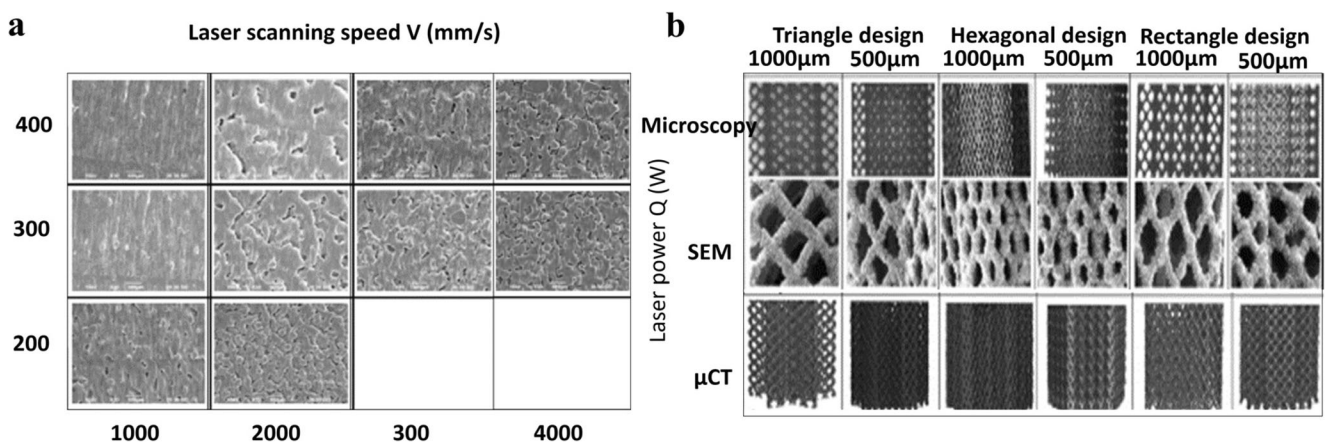

Fig. 15 a SEM images of different laser power and scan speeds of SLM process–made parts [107]. b Microscopic, SEM, and μCT images of Ti6Al4V parts made by SLM [15]

sintered, and metallurgical bonded alloy particles and layers along the build surface. They also observed numerous hemispherical microporosity sizes that range from 6.6 to 8.6 μm [108]. Spierings and his co-authors studied density/porosity of SLM process–made SS 316L parts of different densities (90 to 99.5% density) using microscopy, Archimedes' method, and x-ray analysis. Based on microscopic analysis, the authors observed that porosity increases with laser scanning speed. Higher density (low scan speed) parts show very few spherical pores and moderate scan speed parts show pores through the scan lines. Lastly, higher scan speed parts show pores which are distributed homogeneously with irregular shapes. The higher density (low porosity) samples show no significant difference in porosity with different magnifications, but high porosity (low density) samples show significant difference in different magnifications in microscopic analysis [99]. Valdez and his team also observed similar results with the SEM analysis for Inconel 718 parts made by DMLS process. Density of these parts decreases with decreasing DMLS energy density. SEM images revealed process-induced porosity resembles an open cell foam. μCT scan results show induced porosity is continuous throughout the part [109]. Seo et al. fabricated (laser deposited) open and closed porous Ti64 structures by foaming of melts using TiH_2. Optical microscopy images of polished surfaces showed the open-cell and closed-cell pores formed at different locations within the part. Upon analysis of processing parameters related to the deposition process on the open/closed porosity of the parts, the authors concluded that track spacing parameter during deposition controlled the open porosity and quantity of TiH_2 (foaming agent) controlled the closed porosity [110].

Highly porous 3D-printed $LiFePO_4$ electrode microstructures were characterized by Liu et al. using the SEM analysis and observed a large number of pores having more than the 1 μm diameter on electrode surface as well as a cross section. The pores and voids between $LiFePO_4$ particles provide space for an electrolyte which plays a crucial role in electrochemical performance [67]. Xiong et al. used the SEM analysis to study the porous Ti implants made by 3D printing. The micrographs showed porosity changing from visible macroporous to coral-like microstructure before and after sintering with a pore size between 50 and 150 μm. The study also revealed that porosity decreases with increasing sintering temperature, and at lower sintering temperatures, pores are larger and have a high degree of interconnectivity [33]. The main drawback of microscopic analysis is that the analysis provides only localized porosity values, which may not be representative of the overall porosity of sample. Generally, image analysis software is being used for optical microscopic porosity measurement. In this method, porosity is defined as the ratio of pore volume (number of pixels belongs to the pore space) over the total volume (number of pixels belongs to total image).

4.5 X-ray computed tomography scanning method

The on-growing demand of irregular complex structures for safety-critical applications has increasingly led to the adoption of a nondestructive tool X-ray CT to assess the external and internal features of a component [111]. X-ray CT refers to computerized x-ray imaging procedure, in which X-rays are aimed at sampling and collecting the x-ray images of samples from 0 to 360°. Reconstruction of the volume model can take places out of the acquired 2D gray-level images (slices) of the samples. Then, these slices are computationally piled to produce a 3D view of the sample. As reported in many works of literature, XCT gives full 3D information about the shape, size, and distribution of internal voids and micro- and macroporous structures [4, 39]. But the accuracy of this porosity measurement is still subjective. Butscher et al. proposed and analyzed the relation between different scaffold designs and de-powdering efficiency by using X-ray μCT scanning analysis. With μCT scan data, quantification of mobile fillers was significantly improved. In addition to this, μCT analysis also measures the de-powdering efficiency by calculating the printed volume density of porous scaffolds [107, 112]. Farzadi et al. studied the relation between dimensional exactness and mechanical properties of 3D-printed calcium sulfate–based powder (ZP150) and printing layer delay time. The X-ray μCT analysis was utilized to measure the total porosity and macropore volume of 300-ms delay time printed sample and reported porosity and pore volume of 49.59% and 169.04 mm^3 respectively [39].

As reported by James et al., a significant deviation of overall porosity in SLM AlSi10Mg parts can be observed when compared with Archimedes' micrograph analysis because some pores are smaller than the minimum detectable size [113]. Zanini and his team investigated on the deviation of XCT scan porosity results from other porosity evaluation methods. XCT scanning analysis was performed on SLM-made Ti6Al4V tensile samples, and it was concluded that pore volume errors meaningfully decrease when the pore diameter/voxel size ratio is above 6 [114], whereas Kim et al. used XCT for gravimetric analysis to get the accurate porosity and pore volume to investigate the pore structure and pore defects of AM parts. Local thresholding algorithms were applied on DMLS Co-Cr alloys for selecting a threshold for image analysis. By using this local thresholding technique, quantitative information of porosity, pore size distribution, and virtual removal of trapped powders inside the pores were observed [115].

Usually, trapped powders inside the pores mislead the gravimetric porosity analysis results. This issue overcomes by X-ray analysis. X-ray (CT) analysis is effective when there is an

absorption difference between the different parts of the sample and X-rays able to penetrate completely through the sample with a minimum amount of (10%) transmission. If there are differences in absorption among different parts of the sample, decent images will be formed. Image pixel size (voxels) is one of the important parameters in X-ray CT. If the voxel size is larger than the pore size, pores are not visible in reconstructed images [116]. A balance needs to be taken during the x-ray scan among the resolution, image data size, and time to scan. Generally, it is observed that a higher resolution leads to a longer scan time and bigger size data. In 3D images, air gaps (pores) and bulk material have their specific gray values depending on the X-ray absorption. After the image collection, 3D image is constructed by using a special software to analyze the images and calculate the porosity. This method not only measures the porosity but also analyzes the position, shapes, and size of the pores. For fine micron-level pores and crack detection, X-ray micro-CT scanning is required for high resolution. Porosity measurement of metallic samples by XCT method is not completely understood and sometimes not as accurate as the established Archimedes' method. However, XCT is a more reliable nondestructive test method currently available for pore distribution evaluation in parts [117].

4.6 Permeability measurement

As we are aware that in porous applications, permeability is one of the important factors which measures the pressure drops across the part during fluid/gas flow [118], this permeability is depending not only on the porosity but also on mean pore size and microstructure. The permeability is calculated by Darcy's law where the permeability of porous structure was measured by injecting the deionized water or gas through the test samples at various flow rates and measures the corresponding pressure drop across the porous sample. Once the pressure drop is logged, the permeability is calculated by the following formula:

$$\text{Darcy's equation}: \mu = \frac{V}{t} \; \eta \; \frac{\delta}{A} \; \frac{1}{p_{1-p_2}}$$

whereas μ is the permeability of the porous sample, V/t is the volume of compressed gas or water per unit of time that is passed through the samples, η is the viscosity of the compressed gas or water, and A is the cross-sectional area of the porous sample that facing the compressed media (water or gas). p_1 and p_2 are the pressures of chamber 1 and chamber 2 respectively [107, 119]. Darcy's equation is a theoretically and experimentally valid for laminar flow of medium for all porous media [120]. Furumoto et al. measured the permeability of metal alloy samples made by laser sintering using Darcy's law and reported that permeability of porous structure depending on porosity and permeability increases with

increasing porosity [107]. In contrast to this study, Mengxue et al. studied the porosity and permeability of SLS-made samples and observed a continual increase of permeability with increasing layer thickness while no increase in actual porosity. However, there is no increase in actual porosity. Permeability is strongly influenced by mean pore size and microstructure [14]. Verlee and his team studied the combination of particle shape that used in AM process, pore size, and open porosity on permeability. Nonspherical powders reduce the permeability and lower the pore size, and open porosity impairs the permeability [35].

5 Future challenges and conclusions

The paper provides insight information on AM process for porous applications and discussed in detail about their classifications. GUP is nonuniform and naturally arises as a consequence of AM process parameter optimization for below 100-μm pore size, whereas GDLSP is a macroscopic void space between struts in a lattice design with a controlled uniform porosity with a pore size above 200 μm. Further division of GDLSP into uniform, gradient porosity, and different lattice design (topology selection) structures are mentioned briefly. Different AM process parameter optimizations to get GUP and different lattice design structures for GDLSP were discussed in detail. One of the main observations is that when compared with GDLSP, only a few materials and processes were attempted for GUP-type porosity. One of the major challenges is to apply the most convenient GUP type of porosity for a wide range of materials and to obtain required pore size and porosity below 100 μm.

In GDLSP type of porosity, no universal rule for selecting the unit cell type for porous design has been formulated yet. It is much crucial need to have a universal rule to select "unit cell" for 3D design. Still, based on designs, it is very difficult to fabricate a material of a pore size below 100 μm with interconnected porosity. Also, it was observed a very limited study has been done on a combination of the two types, i.e., GUP and GDLSP, of porosity designs.

Finally, no single kind of porosity characterization method gives full information of pore size, shape, porosity, and permeability. A universal porous characterization method is required for characterizing the AM porous structures to get the full information of porous parts.

References

1. Vaezi M, Seitz H, Yang S (2013) A review on 3D micro-additive manufacturing technologies. Int J Adv Manuf Technol 67(5): 1721–1754. https://doi.org/10.1007/s00170-012-4605-2

2. Delgado Camacho D, Clayton P, O'Brien WJ, Seepersad C, Juenger M, Ferron R, Salamone S (2018) Applications of additive manufacturing in the construction industry – a forward-looking review. Autom Constr 89:110–119. https://doi.org/10.1016/j. autcon.2017.12.031

3. Bose S, Ke D, Sahasrabudhe H, Bandyopadhyay A (2018) Additive manufacturing of biomaterials. Prog Mater Sci 93:45–111. https://doi.org/10.1016/j.pmatsci.2017.08.003

4. Markl D, Strobel A, Schlossnikl R, Bøtker J, Bawuah P, Ridgway C, Rantanen J, Rades T, Gane P, Peiponen K-E, Zeitler JA (2018) Characterisation of pore structures of pharmaceutical tablets: a review. Int J Pharm 538(1):188–214. https://doi.org/10.1016/j. ijpharm.2018.01.017

5. Kang H-W, Park JH, Kang T-Y, Seol Y-J, Cho D-W (2012) Unit cell-based computer-aided manufacturing system for tissue engineering. Biofabrication 4(1):1–8. https://doi.org/10.1088/1758-5082/4/1/015005

6. Zhang X-Y, Fang G, Zhou J (2017) Additively manufactured scaffolds for bone tissue engineering and the prediction of their mechanical behavior: a review. Materials 10(1):50. https://doi.org/10.3390/ma10010050

7. Ker Chin A, Kah Fai L, Chee Kai C, Margam C (2006) Investigation of the mechanical properties and porosity relationships in fused deposition modelling-fabricated porous structures. Rapid Prototyp J 12(2):100–105. https://doi.org/10.1108/13552540610652447

8. Torres-Sanchez C, Al Mushref FRA, Norrito M, Yendall K, Liu Y, Conway PP (2017) The effect of pore size and porosity on mechanical properties and biological response of porous titanium scaffolds. Mater Sci Eng C 77:219–228. https://doi.org/10.1016/j.msec.2017.03.249

9. Kurgan N (2014) Effect of porosity and density on the mechanical and microstructural properties of sintered 316L stainless steel implant materials. Mater Des 55:235–241. https://doi.org/10.1016/j.matdes.2013.09.058

10. El-Hajje A, Kolos EC, Wang JK, Maleksaeedi S, He Z, Wiria FE, Choong C, Ruys AJ (2014) Physical and mechanical characterisation of 3D-printed porous titanium for biomedical applications. J Mater Sci Mater Med 25(11):2471–2480. https://doi.org/10.1007/s10856-014-5277-2

11. Lee J-W, Lee J-S, Kim M-G, Hyun S-K (2013) Fabrication of porous titanium with directional pores for biomedical applications. Mater Trans 54(2):137–142. https://doi.org/10.2320/matertrans. MC201211

12. Ishizaki K, Komarneni S, Nanko M (1998) Applications of porous materials. In: Porous materials: process technology and applications. Springer US, Boston, MA, pp 181–201. https://doi.org/10.1007/978-1-4615-5811-8_5

13. Stoffregen H, Fischer J, Siedelhofer C, Abele E (2011) Selective laser melting of porous structures.

14. Yan M, Tian X, Peng G, Cao Y, Li D (2017) Hierarchically porous materials prepared by selective laser sintering. Mater Des 135:62–68. https://doi.org/10.1016/j.matdes.2017.09.015

15. Van Bael S, Chai YC, Truscello S, Moesen M, Kerckhofs G, Van Oosterwyck H, Kruth JP, Schrooten J (2012) The effect of pore geometry on the in vitro biological behavior of human periosteum-derived cells seeded on selective laser-melted Ti6Al4V bone scaffolds. Acta Biomater 8(7):2824–2834. https://doi.org/10.1016/j.actbio.2012.04.001

16. Cheah CM, Chua CK, Leong KF, Chua SW (2003) Development of a tissue engineering scaffold structure library for rapid prototyping. Part 2: parametric library and assembly program. Int J Adv Manuf Technol 21(4):302–312. https://doi.org/10.1007/s001700300035

17. Cheah CM, Chua CK, Leong KF, Chua SW (2003) Development of a tissue engineering scaffold structure library for rapid prototyping. Part 1: investigation and classification. Int J Adv Manuf Technol 21(4):291–301. https://doi.org/10.1007/s001700300034

18. An J, Teoh JEM, Suntornnond R, Chua CK (2015) Design and 3D printing of scaffolds and tissues. Engineering 1(2):261–268. https://doi.org/10.15302/J-ENG-2015061

19. Egan PF, Gonella VC, Engensperger M, Ferguson SJ, Shea K (2017) Computationally designed lattices with tuned properties for tissue engineering using 3D printing. PLoS One 12(8): e0182902. https://doi.org/10.1371/journal.pone.0182902

20. Amin Yavari S, Ahmadi SM, Wauthle R, Pouran B, Schrooten J, Weinans H, Zadpoor AA (2015) Relationship between unit cell type and porosity and the fatigue behavior of selective laser melted meta-biomaterials. J Mech Behav Biomed Mater 43:91–100. https://doi.org/10.1016/j.jmbbm.2014.12.015

21. Li SJ, Xu QS, Wang Z, Hou WT, Hao YL, Yang R, Murr LE (2014) Influence of cell shape on mechanical properties of Ti–6Al–4V meshes fabricated by electron beam melting method. Acta Biomater 10(10):4537–4547. https://doi.org/10.1016/j.actbio.2014.06.010

22. Ghouse S, Babu S, Van Arkel RJ, Nai K, Hooper PA, Jeffers JRT (2017) The influence of laser parameters and scanning strategies on the mechanical properties of a stochastic porous material. Mater Des 131:498–508. https://doi.org/10.1016/j.matdes.2017.06.041

23. Xiao L, Song W (2018) Additively-manufactured functionally graded Ti-6Al-4V lattice structures with high strength under static and dynamic loading: experiments. Int J Impact Eng 111:255–272. https://doi.org/10.1016/j.ijimpeng.2017.09.018

24. Nune KC, Kumar A, Misra RDK, Li SJ, Hao YL, Yang R (2017) Functional response of osteoblasts in functionally gradient titanium alloy mesh arrays processed by 3D additive manufacturing. Colloids Surf B: Biointerfaces 150:78–88. https://doi.org/10.1016/j.colsurfb.2016.09.050

25. Khoda AKM, Ozbolat IT, Koc B (2013) Designing heterogeneous porous tissue scaffolds for additive manufacturing processes. Comput Aided Des 45(12):1507–1523. https://doi.org/10.1016/j.cad.2013.07.003

26. Contuzzi N, Campanelli SL, Caiazzo F, Alfieri V (2019) Design and fabrication of random metal foam structures for laser powder bed fusion. Materials 12(8):1301. https://doi.org/10.3390/ma12081301

27. Sachs E, Cima M, Cornie J (1990) Three-dimensional printing: rapid tooling and prototypes directly from a CAD model. CIRP Ann 39(1):201–204. https://doi.org/10.1016/S0007-8506(07)61035-X

28. Gibson I, Rosen D, Stucker B (2015) Additive manufacturing technologies. Springer. https://doi.org/10.1007/978-1-4939-2113-3

29. Salehi M, Gupta M, Maleksaeedi S, Sharon NML (2018) Inkjet based 3D additive manufacturing of metals, vol 20. Mater Res Solid State Phys Eng. https://doi.org/10.21741/9781945291456

30. Wang Y, Zhao YF (2017) Investigation of sintering shrinkage in binder jetting additive manufacturing process. Procedia Manufacturing 10:779–790. https://doi.org/10.1016/j.promfg.2017.07.077

31. Kiran ASK, Veluru JB, Merum S, Radhamani AV, Doble M, Kumar TSS, Ramakrishna S (2018) Additive manufacturing technologies: an overview of challenges and perspective of using electrospraying. Nanocomposites 4(4):190–214. https://doi.org/10.1080/20550324.2018.1558499

32. Turker M, Godlinski D, Petzoldt F (2008) Effect of production parameters on the properties of IN 718 superalloy by three-dimensional printing. Mater Charact 59(12):1728–1735. https://doi.org/10.1016/j.matchar.2008.03.017

33. Xiong Y, Qian C, Sun J (2012) Fabrication of porous titanium implants by three-dimensional printing and sintering at different temperatures. Dent Mater J 31(5):815–820. https://doi.org/10.4012/dmj.2012-065

34. Ziaee M, Tridas EM, Crane NB (2017) Binder-jet printing of fine stainless steel powder with varied final density. JOM 69(3):592–596. https://doi.org/10.1007/s11837-016-2177-6

35. Verlee B, Dormal T, Lecomte-Beckers J (2012) Density and porosity control of sintered 316L stainless steel parts produced by additive manufacturing. Powder Metall 55(4):260–267. https://doi.org/10.1179/0032589912Z.00000000082

36. Miguel C, Barbara G, Inês P, Jorge R, Manuel P (2015) The role of shell/core saturation level on the accuracy and mechanical characteristics of porous calcium phosphate models produced by 3D printing. Rapid Prototyp J 21(1):43–55. https://doi.org/10.1108/RPJ-02-2013-0015

37. Zhang W, Melcher R, Travitzky N, Bordia RK, Greil P (2009) Three-dimensional printing of complex-shaped alumina/glass composites. Adv Eng Mater 11(12):1039–1043. https://doi.org/10.1002/adem.200900213

38. Asadi-Eydivand M, Solati-Hashjin M, Farzad A, Abu Osman NA (2016) Effect of technical parameters on porous structure and strength of 3D printed calcium sulfate prototypes. Robot Comput Integr Manuf 37:57–67. https://doi.org/10.1016/j.rcim.2015.06.005

39. Farzadi A, Waran V, Solati-Hashjin M, Rahman ZAA, Asadi M, Osman NAA (2015) Effect of layer printing delay on mechanical properties and dimensional accuracy of 3D printed porous prototypes in bone tissue engineering. Ceram Int 41(7):8320–8330. https://doi.org/10.1016/j.ceramint.2015.03.004

40. Vangapally S, Agarwal K, Sheldon A, Cai S (2017) Effect of lattice design and process parameters on dimensional and mechanical properties of binder jet additively manufactured stainless steel 316 for bone scaffolds. Procedia Manufacturing 10:750–759. https://doi.org/10.1016/j.promfg.2017.07.069

41. Suwanprateeb J, Chumnanklang R (2006) Three-dimensional printing of porous polyethylene structure using water-based binders. J Biomed Mater Res B Appl Biomater 78B(1):138–145. https://doi.org/10.1002/jbm.b.30469

42. Hong D, Chou D-T, Velikokhatnyi OI, Roy A, Lee B, Swink I, Issaev I, Kuhn HA, Kumta PN (2016) Binder-jetting 3D printing and alloy development of new biodegradable Fe-Mn-Ca/Mg alloys. Acta Biomater 45:375–386. https://doi.org/10.1016/j.actbio.2016.08.032

43. Seitz H, Rieder W, Irsen S, Leukers B, Tille C (2005) Three-dimensional printing of porous ceramic scaffolds for bone tissue engineering. J Biomed Mater Res B Appl Biomater 74B(2):782–788. https://doi.org/10.1002/jbm.b.30291

44. Spears TG, Gold SA (2016) In-process sensing in selective laser melting (SLM) additive manufacturing. Integr Mater Manuf Innov 5(1). https://doi.org/10.1186/s40192-016-0045-4

45. Gu DD, Meiners W, Wissenbach K, Poprawe R (2012) Laser additive manufacturing of metallic components: materials, processes and mechanisms. Int Mater Rev 57(3):133–164. https://doi.org/10.1179/1743280411Y.0000000014

46. Bikas H, Stavropoulos P, Chryssolouris G (2016) Additive manufacturing methods and modelling approaches: a critical review. Int J Adv Manuf Technol 83(1):389–405. https://doi.org/10.1007/s00170-015-7576-2

47. Kruth JP, Levy G, Klocke F, Childs THC (2007) Consolidation phenomena in laser and powder-bed based layered manufacturing. CIRP Ann 56(2):730–759. https://doi.org/10.1016/j.cirp.2007.10.004

48. Shirazi SFS, Gharehkhani S, Mehrali M, Yarmand H, Metselaar HSC, Adib Kadri N, Osman NAA (2015) A review on powder-based additive manufacturing for tissue engineering: selective laser sintering and inkjet 3D printing. Sci Technol Adv Mater 16(3):033502. https://doi.org/10.1088/1468-6996/16/3/033502

49. M.M. S, L. H, P.M. D, Y. Z, K.E. T, R.A. H (2012) The effects and interactions of fabrication parameters on the properties of selective laser sintered hydroxyapatite polyamide composite biomaterials. Rapid Prototyp J 18 (1):16–27. https://doi.org/10.1108/13552541211193467

50. E. TA, T.H.C. C (2001) Density prediction of crystalline polymer sintered parts at various powder bed temperatures. Rapid Prototyp J 7 (3):180–184. doi:https://doi.org/10.1108/13552540110395637

51. Yadroitsev I, Shishkovsky I, Bertrand P, Smurov I (2009) Manufacturing of fine-structured 3D porous filter elements by selective laser melting. Appl Surf Sci 255(10):5523–5527. https://doi.org/10.1016/j.apsusc.2008.07.154

52. Spierings A, Wegener K, Levy G (2012) Designing material properties locally with additive manufacturing technology SLM. https://doi.org/10.3929/ethz-a-010335595

53. Abele E, Stoffregen HA, Kniepkamp M, Lang S, Hampe M (2015) Selective laser melting for manufacturing of thin-walled porous elements. J Mater Process Technol 215:114–122. https://doi.org/10.1016/j.jmatprotec.2014.07.017

54. Gu D (2015) Laser additive manufacturing (AM): classification, processing philosophy, and metallurgical mechanisms. In: Gu D (ed) Laser additive manufacturing of high-performance materials. Springer, Berlin Heidelberg, Berlin, Heidelberg, pp 15–71. https://doi.org/10.1007/978-3-662-46089-4_2

55. Cunningham R, Nicolas A, Madsen J, Fodran E, Anagnostou E, Sangid MD, Rollett AD (2017) Analyzing the effects of powder and post-processing on porosity and properties of electron beam melted Ti-6Al-4V. Mater Res Lett 5(7):516–525. https://doi.org/10.1080/21663831.2017.1340911

56. Bandyopadhyay A, Krishna BV, Xue W, Bose S (2008) Application of laser engineered net shaping (LENS) to manufacture porous and functionally graded structures for load bearing implants. J Mater Sci Mater Med 20(1):29. https://doi.org/10.1007/s10856-008-3478-2

57. Das M, Balla VK, Kumar TSS, Manna I (2013) Fabrication of biomedical implants using Laser Engineered Net Shaping (LENS™). T Indian Ceram Soc 72(3):169–174. https://doi.org/10.1080/0371750X.2013.851619

58. España FA, Balla VK, Bose S, Bandyopadhyay A (2010) Design and fabrication of CoCrMo alloy based novel structures for load bearing implants using laser engineered net shaping. Mater Sci Eng C 30(1):50–57. https://doi.org/10.1016/j.msec.2009.08.006

59. Ngo TD, Kashani A, Imbalzano G, Nguyen KTQ, Hui D (2018) Additive manufacturing (3D printing): a review of materials, methods, applications and challenges. Compos Part B 143:172–196. https://doi.org/10.1016/j.compositesb.2018.02.012

60. Kojima M, Narahara H, Nakao Y, Fukumaru H, Koresawa H, Suzuki H, Abe S (2008) Permeability characteristics and applications of plastic injection molding fabricated by metal laser sintering combined with high speed milling. Int J Autom Technol 2:175–181. https://doi.org/10.20965/ijat.2008.p0175

61. Narahara H, Takeshita S, Fukumaru H, Koresawa H, Suzuki H (2012) Permeability performance on porous structure of injection mold fabricated by metal laser sintering combined with high speed milling. Int J Autom Technol 6(5):576–583. https://doi.org/10.20965/ijat.2012.p0576

62. Jafari D, Wits W, Geurts JB (2017) An investigation of porous structure characteristics of heat pipes made by additive manufacturing. International Workshop on Thermal Investigations of ICs and Systems (THERMINIC) :1–7. https://doi.org/10.1109/THERMINIC.2017.8233841

63. Ameli M, Agnew B, Leung PS, Ng B, Sutcliffe CJ, Singh J, McGlen R (2013) A novel method for manufacturing sintered

aluminium heat pipes (SAHP). Appl Therm Eng 52(2):498–504. https://doi.org/10.1016/j.applthermaleng.2012.12.011

64. Calignano F, Tommasi T, Manfredi D, Chiolerio A (2015) Additive manufacturing of a microbial fuel cell-a detailed study. Sci Rep 5:17373. https://doi.org/10.1038/srep17373

65. Yashiro N, Usui T, Kikuta K (2010) Application of a thin intermediate cathode layer prepared by inkjet printing for SOFCs. J Eur Ceram Soc 30(10):2093–2098. https://doi.org/10.1016/j.jeurceramsoc.2010.04.012

66. Delannoy PE, Riou B, Brousse T, Le Bideau J, Guyomard D, Lestriez B (2015) Ink-jet printed porous composite LiFePO$_4$ electrode from aqueous suspension for microbatteries. J Power Sources 287:261–268. https://doi.org/10.1016/j.jpowsour.2015.04.067

67. Liu C, Cheng X, Li B, Chen Z, Mi S, Lao C (2017) Fabrication and characterization of 3D-printed highly-porous 3D LiFePO$_4$ electrodes by low temperature direct writing process. Materials 10(8):934. https://doi.org/10.3390/ma10080934

68. Wang X, Xu S, Zhou S, Xu W, Leary M, Choong P, Qian M, Brandt M, Xie Y (2016) Topological design and additive manufacturing of porous metals for bone scaffolds and orthopaedic implants: a review. Biomaterials 83:127–141. https://doi.org/10.1016/j.biomaterials.2016.01.012

69. Sun K, Wei T-S, Ahn BY, Seo JY, Dillon SJ, Lewis JA (2013) 3D Printing of interdigitated Li-ion microbattery architectures. Adv Mater 25(33):4539–4543. https://doi.org/10.1002/adma.201301036

70. You J, Preen RJ, Bull L, Greenman J, Ieropoulos I (2017) 3D printed components of microbial fuel cells: towards monolithic microbial fuel cell fabrication using additive layer manufacturing. Sustain Energy Technol Assessments 19:94–101. https://doi.org/10.1016/j.seta.2016.11.006

71. Burns N, Burns M, Travis D, Geekie L, Rennie A, Weston DP (2013) Novel filter designs that deliver filtration benefits produced by metal additive manufacturing. Proceedings of AFS 2013 Fall Conference: Innovation in Filter Media and Membranes:194–217

72. Obaton AF, Fain J, Djemaï M, Meinel D, Léonard F, Mahé E, Lécuelle B, Fouchet JJ, Bruno G (2017) In vivo XCT bone characterization of lattice structured implants fabricated by additive manufacturing. Heliyon 3(8):e00374. https://doi.org/10.1016/j.heliyon.2017.e00374

73. Burns N (2014) Why AM now has the potential to revolutionise filtration solutions. Filtration + Separation 51(2):42–43. https://doi.org/10.1016/S0015-1882(14)70073-4

74. Burns N, Burns M, Travis D, Geekie L, Rennie AEW (2016) Designing advanced filtration media through metal additive manufacturing. Chem Eng Technol 39(3):535–542. https://doi.org/10.1002/ceat.201500353

75. Burns NR, Burns MA, Travis D, Geekie LE, Rennie AEW AM: applications & materials: innovations in filtration through additive manufacturing. In, Shrewsbury, 2014 2014. The European Powder Metallurgy Association, pp 1–6

76. Nandwana P, Kirka M, Okello A, Dehoff R (2018) Electron beam melting of Inconel 718: effects of processing and post-processing. Mater Sci Technol:1–8. https://doi.org/10.1080/02670836.2018.1424379

77. Polonsky AT, Echlin MP, Lenthe WC, Dehoff RR, Kirka MM, Pollock TM Defects and 3D structural inhomogeneity in electron beam additively manufactured Inconel 718. Mater Charact. https://doi.org/10.1016/j.matchar.2018.02.020

78. Low Z-X, Chua YT, Ray BM, Mattia D, Metcalfe IS, Patterson DA (2017) Perspective on 3D printing of separation membranes and comparison to related unconventional fabrication techniques. J Membr Sci 523:596–613. https://doi.org/10.1016/j.memsci.2016.10.006

79. Klahn C, Bechmann F, Hofmann S, Dinkel M, Emmelmann C (2013) Laser additive manufacturing of gas permeable structures. Phys Procedia 41:873–880. https://doi.org/10.1016/j.phpro.2013.03.161

80. Manogharan G, Kioko M, Linkous C (2015) Binder jetting: a novel solid oxide fuel-cell fabrication process and evaluation. JOM 67(3):660–667. https://doi.org/10.1007/s11837-015-1296-9

81. Rahimnejad M, Adhami A, Darvari S, Zirepour A, Oh S-E (2015) Microbial fuel cell as new technology for bioelectricity generation: a review. Alex Eng J 54(3):745–756. https://doi.org/10.1016/j.aej.2015.03.031

82. Bian B, Shi D, Cai X, Hu M, Guo Q, Zhang C, Wang Q, Sun AX, Yang J (2018) 3D printed porous carbon anode for enhanced power generation in microbial fuel cell. Nano Energy 44:174–180. https://doi.org/10.1016/j.nanoen.2017.11.070

83. Zhou Y, Tang L, Liu Z, Hou J, Chen W, Li Y, Sang L (2017) A novel anode fabricated by three-dimensional printing for use in urine-powered microbial fuel cell. Biochem Eng J 124:36–43. https://doi.org/10.1016/j.bej.2017.04.012

84. Zhang F, Wei M, Viswanathan VV, Swart B, Shao Y, Wu G, Zhou C (2017) 3D printing technologies for electrochemical energy storage. Nano Energy 40:418–431. https://doi.org/10.1016/j.nanoen.2017.08.037

85. Liu X, Jervis R, Maher RC, Villar-Garcia IJ, Naylor-Marlow M, Shearing PR, Ouyang M, Cohen L, Brandon NP, Wu B (2016) 3D-printed structural pseudocapacitors. Advanced Materials Technologies 1 (9):1600167-n/a. https://doi.org/10.1002/admt.201600167

86. Azhari A, Marzbanrad E, Yilman D, Toyserkani E, Pope MA (2017) Binder-jet powder-bed additive manufacturing (3D printing) of thick graphene-based electrodes. Carbon 119:257–266. https://doi.org/10.1016/j.carbon.2017.04.028

87. Kumar A, Mandal S, Barui S, Vasireddi R, Gbureck U, Gelinsky M, Basu B (2016) Low temperature additive manufacturing of three dimensional scaffolds for bone-tissue engineering applications: processing related challenges and property assessment. Mater Sci Eng R Rep 103:1–39. https://doi.org/10.1016/j.mser.2016.01.001

88. Esch C, Galperin A, Krolitzki B, Glasmacher B, Shen A, Ratner BD (2013) Proof of concept of a new glucose sensing technology: color-changing hydrogels including Au nanoparticles. Biomedical Engineering/Biomedizinische Technik. https://doi.org/10.1515/bmt-2013-4063

89. Wauthle R, van der Stok J, Amin Yavari S, Van Humbeeck J, Kruth J-P, Zadpoor AA, Weinans H, Mulier M, Schrooten J (2015) Additively manufactured porous tantalum implants. Acta Biomater 14:217–225. https://doi.org/10.1016/j.actbio.2014.12.003

90. Ahmadi SM, Amin Yavari S, Wauthle R, Pouran B, Schrooten J, Weinans H, Zadpoor AA (2015) Additively manufactured open-cell porous biomaterials made from six different space-filling unit cells: the mechanical and morphological properties. Materials 8(4):1871–1896. https://doi.org/10.3390/ma8041871

91. Li JP, Habibovic P, van den Doel M, Wilson CE, de Wijn JR, van Blitterswijk CA, de Groot K (2007) Bone ingrowth in porous titanium implants produced by 3D fiber deposition. Biomaterials 28(18):2810–2820. https://doi.org/10.1016/j.biomaterials.2007.02.020

92. Mour M, Das D, Winkler T, Hoenig E, Mielke G, Morlock MM, Schilling AF (2010) Advances in porous biomaterials for dental and orthopaedic applications. Materials 3(5):2947. https://doi.org/10.3390/ma3052947

93. Bhargav A, Sanjairaj V, Rosa V, Feng LW, Fuh Yh J Applications of additive manufacturing in dentistry: a review. J Biomed Mater Res Part B. https://doi.org/10.1002/jbm.b.33961

94. Traini T, Mangano C, Sammons RL, Mangano F, Macchi A, Piattelli A (2008) Direct laser metal sintering as a new approach to fabrication of an isoelastic functionally graded material for manufacture of porous titanium dental implants. Dent Mater 24(11):1525–1533. https://doi.org/10.1016/j.dental.2008.03.029

95. Cheah CM, Leong KF, Chua CK, Low KH, Quek HS (2002) Characterization of microfeatures in selective laser sintered drug delivery devices. Proc Inst Mech Eng H J Eng Med 216(6):369–383. https://doi.org/10.1243/095441102321032166

96. Fina F, Goyanes A, Gaisford S, Basit AW (2017) Selective laser sintering (SLS) 3D printing of medicines. Int J Pharm 529(1):285–293. https://doi.org/10.1016/j.ijpharm.2017.06.082

97. Ma J (2015) Review of permeability evolution model for fractured porous media. J Rock Mech Geotech Eng 7(3):351–357. https://doi.org/10.1016/j.jrmge.2014.12.003

98. Monzón MD, Ortega Z, Martínez A, Ortega F (2015) Standardization in additive manufacturing: activities carried out by international organizations and projects. Int J Adv Manuf Technol 76(5):1111–1121. https://doi.org/10.1007/s00170-014-6334-1

99. Spierings AB, Schneider M, Eggenberger R (2011) Comparison of density measurement techniques for additive manufactured metallic parts. Rapid Prototyp J 17(5):380–386. https://doi.org/10.1108/13552541111156504

100. Williams CB, Cochran JK, Rosen DW (2011) Additive manufacturing of metallic cellular materials via three-dimensional printing. Int J Adv Manuf Technol 53(1):231–239. https://doi.org/10.1007/s00170-010-2812-2

101. Slotwinski JA, Garboczi EJ, Hebenstreit KM (2014) Porosity measurements and analysis for metal additive manufacturing process control. J Res Natl Inst Stand Technol 119:494–528. https://doi.org/10.6028/jres.119.019

102. Manfredi D, Calignano F, Ambrosio EP, Krishnan M, Canali R, Biamino S, Pavese M, Atzeni E, Iuliano L, Fino P, Badini C (2013) Direct metal laser sintering: an additive manufacturing technology ready to produce lightweight structural parts for robotic applications. La Metallurgia Italiana 10:15–24

103. Paul CP, Mishra SK, Premsingh CH, Bhargava P, Tiwari P, Kukreja LM (2012) Studies on laser rapid manufacturing of cross-thin-walled porous structures of Inconel 625. Int J Adv Manuf Technol 61(5):757–770. https://doi.org/10.1007/s00170-011-3742-3

104. Giesche H (2006) Mercury porosimetry: a general (practical) overview. Part Part Syst Charact 23(1):9–19. https://doi.org/10.1002/ppsc.200601009

105. Jande YAC, Erdal M, Dag S (2014) Production of graded porous polyamide structures and polyamide-epoxy composites via selective laser sintering. J Reinf Plast Compos 33(11):1017–1036. https://doi.org/10.1177/0731684414522536

106. Kim TB, Yue S, Zhang Z, Jones E, Jones JR, Lee PD (2014) Additive manufactured porous titanium structures: through-process quantification of pore and strut networks. J Mater Process Technol 214(11):2706–2715. https://doi.org/10.1016/j.jmatprotec.2014.05.006

107. Furumoto T, Koizumi A, Alkahari MR, Anayama R, Hosokawa A, Tanaka R, Ueda T (2015) Permeability and strength of a porous metal structure fabricated by additive manufacturing. J Mater Process Technol 219:10–16. https://doi.org/10.1016/j.jmatprotec.2014.11.043

108. Ramakrishnaiah R, Al kheraif AA, Mohammad A, Divakar DD, Kotha SB, Celur SL, Hashem MI, Vallittu PK, Rehman IU (2017) Preliminary fabrication and characterization of electron beam melted Ti–6Al–4V customized dental implant. Saudi J Biol Sci 24(4):787–796. https://doi.org/10.1016/j.sjbs.2016.05.001

109. Valdez M, Kozuch C, Faierson EJ, Jasiuk I (2017) Induced porosity in Super Alloy 718 through the laser additive manufacturing process: microstructure and mechanical properties. J Alloys Compd 725:757–764. https://doi.org/10.1016/j.jallcom.2017.07.198

110. Seo J-Y, Shim D-S (2018) Effect of track spacing on porosity of metallic foam fabricated by laser melting deposition of Ti6Al4V/TiH2 powder mixture. Vacuum 154:200–207. https://doi.org/10.1016/j.vacuum.2018.04.058

111. Kruth JP, Bartscher M, Carmignato S, Schmitt R, De Chiffre L, Weckenmann A (2011) Computed tomography for dimensional metrology. CIRP Ann 60(2):821–842. https://doi.org/10.1016/j.cirp.2011.05.006

112. Butscher A, Bohner M, Doebelin N, Hofmann S, Müller R (2013) New depowdering-friendly designs for three-dimensional printing of calcium phosphate bone substitutes. Acta Biomater 9(11):9149–9158. https://doi.org/10.1016/j.actbio.2013.07.019

113. Damon J, Dietrich S, Vollert F, Gibmeier J, Schulze V (2018) Process dependent porosity and the influence of shot peening on porosity morphology regarding selective laser melted AlSi10Mg parts. Addit Manuf 20:77–89. https://doi.org/10.1016/j.addma.2018.01.001

114. Zanini F, Sbettega E, Carmignato S (2018) X-ray computed tomography for metal additive manufacturing: challenges and solutions for accuracy enhancement. Procedia CIRP 75:114–118. https://doi.org/10.1016/j.procir.2018.04.050

115. Kim FH, Moylan SP, Garboczi EJ, Slotwinski JA (2017) Investigation of pore structure in cobalt chrome additively manufactured parts using X-ray computed tomography and three-dimensional image analysis. Addit Manuf 17:23–38. https://doi.org/10.1016/j.addma.2017.06.011

116. Ziółkowski G, Chlebus E, Szymczyk P, Kurzac J (2014) Application of X-ray CT method for discontinuity and porosity detection in 316L stainless steel parts produced with SLM technology. Arch Civil Mech Eng 14(4):608–614. https://doi.org/10.1016/j.acme.2014.02.003

117. Thompson A, Maskery I, Leach RK (2016) X-ray computed tomography for additive manufacturing: a review. Meas Sci Technol 27(7):072001. https://doi.org/10.1088/0957-0233/27/7/072001

118. Childs EC, Collis-George N (1950) The permeability of porous materials. Proceedings of the Royal Society of London Series A Mathematical and Physical Sciences 201(1066):392–405. https://doi.org/10.1098/rspa.1950.0068

119. Joseph J, Siva Kumar Gunda N, Mitra SK (2013) On-chip porous media: porosity and permeability measurements. Chem Eng Sci 99:274–283. https://doi.org/10.1016/j.ces.2013.05.065

120. Pal L, Joyce MK, Fleming P (2006) A simple method for calculation of the permeability coefficient of porous media. TAPPI J 5